A search for flavour changing neutral currents involving a top quark and a Z boson, using the data collected by the CMS collaboration at a centre of mass of 13 TeV

Van Parijs, Isis

Proefschrift ingediend met het oog op het behalen van de academische graad Doctor in de Wetenschappen.

Published in Faculteit Wetenschappen & Bio-ingenieurswetenschappen
Vrije Universiteit Brussel
At 1. June 2017.

Responsible Contact: I. Van Parijs
Intitute for High Energy Physics
Promotor: Prof. Jorgen D'Hondt

First Referee:	Prof. Dr. J. D’Hondt
Date of Hand-in:	10 November 2017
Date of Defense:	10 December 2017

Contents

1 Theoretical basis

The Standard Model (SM) [1] is a name given in 1970s to a theory describing the fundamental particles and their interactions. This quantum field theory describes the particles and their interactions as fields and has successfully incorporated three of the four fundamental forces in the universe. In Section 1.1, the particle content of the SM is summarised, while Section 1.2 describes the SM Lagrangian and its symmetries. In Section 1.3, the flavour content of the SM is highlighted. The successful theory of the SM has some shortcomings which are discussed in Section 1.4 and lead to searches for a more general theory. One of such a search is using effective field theory (EFT). In Section 1.5 an EFT model focussing on flavour changing neutral currents (FCNC) involving a top quark is presented. Its current experimental constraints are given in Section 1.6.

The physics search presented in this thesis relies on statistical tools and interpretations. In Section **??**, the notion of a likelihood is presented as well as maximum likelihood fits. To set upper limits on a signal process the confidence levels method is used. The background modelling is checked using goodness-of-fit tests. Furthermore, the search will use multivariate analysis methods which are also explained.

1.1 Elementary particles and forces

The interactions in nature can be described by four forces, the strong force, the electromagnetic (EM) force, the weak force and the gravitational force. These interactions happpen via particles with an integer spin known as bosons. The strong interaction is mediated by eight gluons g, while the electromagnetic force is mediated by photons γ, and the weak force by Z and $\mathrm{W}^{\pm}$ bosons. In Table 1.1, the forces and their characteristics are shown. The gravitational force is the only force not included in the SM and can be neglected for energies lower than the Planck scale ($1.22\ 10^{19}$ GeV).

The fermions are the particles that make up the visible matter in the universe. They carry half integer spin and can be subdivided into leptons and quarks, where leptons don't interact strongly. Each fermion has a corresponding anti-fermion which has the same mass and is oppositely charged. The electron e^{-} is the first elementary particle discovered [2] and belongs to the first generation of leptons together with electron neutrino ν_{e}. The second generation is made up

Table 1.1: The four forces of nature and their characteristics.

	Range	Mediator
Strong force	10^{e}—15 m	8 gluons
Electromagnetic force	∞	photon
Weak force	10^{-18} m	$W^{\pm}$, Z bosons
Gravitational force	∞	unknown

of the muon μ^- and the muon neutrino ν_μ, whereas the third generation consists of the tau τ and the tau neutrino ν_τ. The neutrino's are neutral particles, while the other leptons have charge $\pm q_\mathrm{e}$ where q_e represents the elementary charge of $1.602\ 10^{-19}$ C. The masses of the charged leptons differ by four orders of magnitude between the first and third generations.In the SM the neutrino's are assumed to be massless, while it is experimentally established that neutrino do have a tiny non-zero mass. In Table 1.2, the leptons and their properties in the SM are summarised.

Table 1.2: The properties of the leptons in the three generations of the SM [3], where q_e represents the elementary charge.

Generation	Particle	Mass	Charge
First	e^-	0.511 MeV	-q_e
	ν_e	≈ 0	0
Second	μ^-	106 MeV	-q_e
	ν_μ	≈ 0	0
Third	τ	1 777 MeV	-q_e
	ν_τ	≈ 0	0

The quarks can also be divided into three generations. Unlike the leptons, they carry colour charge and can interact via the strong interaction. The top quark, discovered in 1995 at the Tevatron [4, 5] is the heaviest SM particle with a mass close to 173.1 ± 0.6 GeV[1] [3]. The quarks and their properties are summarized in Table 1.3. In nature, only colour neutral objects can exist. This has as consequence that quarks are bound through gluons into mesons (quark+anti-quark) and baryons (three quarks). These mesons and baryons are mostly short-lived and unstable particle that rapidly decay through $W^{\pm}$ and Z bosons, associated with a fermion. The only known stable baryon is the proton, made up of two up quarks and one down quark.

The scalar boson, commonly known as the Higgs boson, is the last piece of the SM and is discovered in 2012 [6, 7]. It is responsible for the masses of the $W^{\pm}$ and Z boson, and that of the fermions.

[1] In this thesis all masses and energies are expressed in natural units, where the speed of light and $\hbar$ are taken to be equal to one.

Table 1.3: The properties of the quarks in the three generations of the SM [3], where q_{e} represents the elementary charge.

Generation	Particle	Mass	Charge
First	up u	$2.2^{+0.6}_{-0.4}$ MeV	$\frac{2}{3}\,q_{\mathrm{e}}$
	down d	$4.7^{+0.5}_{-0.4}$ MeV	$\frac{-1}{3}\,q_{\mathrm{e}}$
Second	charm c	1.28 ± 0.03 GeV	$\frac{2}{3}\,q_{\mathrm{e}}$
	strange s	96^{+8}_{-4} MeV	$\frac{-1}{3}\,q_{\mathrm{e}}$
Third	top t	173.1 ± 0.6 GeV	$\frac{2}{3}\,q_{\mathrm{e}}$
	bottom b	$4.18^{+0.04}_{-0.03}$ GeV	$\frac{-1}{3}\,q_{\mathrm{e}}$

1.2 Standard Model Lagrangian

The SM is a quantum field theory and thus describes the dynamics and kinematics of particles and forces by a Lagrangian $\mathscr{L}$. The theory is based on the $\mathrm{SU_C}(3) \times \mathrm{SU_L}(2) \times \mathrm{U_Y}(1)$ gauge symmetry, where $\mathrm{SU_L}(2) \times \mathrm{U_Y}(1)$ describes the electroweak interaction and $\mathrm{SU_C}(3)$ the strong coupling. The indices refer to colour C, the left chiral nature of the $\mathrm{SU_L}(2)$ coupling L, and the weak hypercharge Y. Its Lagrangian is constructed such that contains symmetries representing physics conservation laws such as conservation of energy, momentum and angular momentum. By imposing gauge invariance the symmetries under local group transformations are sustained.

NOTE: should I explain gauge invariance or is a reference enough?

The $\mathrm{U_Y}(1)$ group has one generator Y with an associated gauge field B_μ. The three gauge fields W^1_μ, W^2_μ, and W^3_μ, are associated to $\mathrm{SU_L}(2)$with three generators that can can be written as half of the Pauli matrices:

$$T_1 = \frac{1}{2}\begin{pmatrix} 0 & 1 \\ 1 & 0 \end{pmatrix},\ T_2 = \frac{1}{2}\begin{pmatrix} 0 & -i \\ i & 0 \end{pmatrix},\ \text{and } T_3 = \frac{1}{2}\begin{pmatrix} 1 & 0 \\ 0 & -1 \end{pmatrix}. \tag{1.1}$$

The generators T^a satisfy the Lie algebra:

$$\left[T^a, T^b\right] = i\epsilon^{abc}T_c \text{ and} \left[T^a, Y\right] = 0, \tag{1.2}$$

where ϵ^{abc} is an antisymmetric tensor. The gauge fields of $\mathrm{SU_L}(2)$ only couple to left-handed fermions as required by the observed parity violating nature of the weak force. The $\mathrm{SU_C}(3)$ group represents quantum chromodynamics (QCD). It has eight generators corresponding to eight gluon fields $\mathrm{G}^{1\ldots8}_\mu$. Unlike $\mathrm{SU_L}(2) \times \mathrm{U_Y}(1)$, $\mathrm{SU_C}(3)$ is not chiral.

Under $\mathrm{SU_C}(3)$ quarks are colour triplets while leptons are colour singlets. This implies that the quarks carry a colour index ranging between one and three, whereas leptons do not take part in strong interactions. Based on the chirality, the quarks and leptons are organized in doublets or singlets. Each generation i of fermions consists of left-handed doublets and right-handed singlets:

$$\mathrm{l_L} = \begin{pmatrix} \mathrm{e^-}_\mathrm{L} \\ \nu_\mathrm{L} \end{pmatrix},\ \mathrm{e^-}_\mathrm{R},\ \mathrm{q_L} = \begin{pmatrix} \mathrm{u_L} \\ \mathrm{d_L} \end{pmatrix},\ \mathrm{u_R},\ \text{and } \mathrm{d_R} \tag{1.3}$$

The SM Lagrangian can be decomposed as a sum of four terms

$$\mathscr{L}_{\mathrm{SM}} = \mathscr{L}_{\mathrm{gauge}} + \mathscr{L}_{\mathrm{f}} + \mathscr{L}_{\mathrm{Yuk}} + \mathscr{L}_{\phi}, \tag{1.4}$$

that are related to the gauge, fermion, Yukawa and scalar sectors. The gauge Lagrangian regroups the gauge fields of all three symmetry groups, and the fermionic part consists of kinetic energy terms for quarks and leptons. The interaction between fermions and the scalar doublet ϕ gives rise to fermion masses and is described by the Yukawa Lagrangian. The scalar part of the Lagrangian is composed of a kinematic and potential component related to the scalar boson.

For the electroweak theory, two coupling constants are introduced, namely g' for $\mathrm{U_Y}(1)$ and g for $\mathrm{SU_L}(2)$. The physically observable gauge bosons of this theory are the photon field A_μ, the Z boson field Z^0_μ, and the W field $\mathrm{W}^\pm_\mu$. These are a superposition of the four gauge fields of $\mathrm{SU_L}(2) \times \mathrm{U_Y}(1)$:

$$\mathrm{A}_\mu = \sin\theta_\mathrm{W} \mathrm{W}^1_\mu + \cos\theta_\mathrm{W} \mathrm{B}_\mu,\ \mathrm{Z}^0_\mu = \cos\theta_\mathrm{W} \mathrm{W}^3_\mu - \sin\theta_\mathrm{W} \mathrm{B}_\mu,\ \text{and } \mathrm{W}^\pm_\mu = \sqrt{\frac{1}{2}}\left(\mathrm{W}^1_\mu \mp \mathrm{W}^2_\mu\right), \tag{1.5}$$

where θ_W represents the weak mixing angle defined as $\tan\theta_\mathrm{W} = \frac{g'}{g}$.

The coupling constant representing the strength of the QCD interactions is denoted as g_s. In QCD their is asymptotic freedom whereby the strong coupling constant becomes weaker as the energy with which the interaction between strongly interacting particles is probed increases, and stronger as the distance between the particles increases. A consequence of this is known as colour confinement. The quarks and gluons can not exist on their own and are not observed individually. They are bound in colour neutral states called hadrons, this process is known as hadronisation.

Electroweak symmetry breaking

In $\mathscr{L}_{\mathrm{gauge}}$ and $\mathscr{L}_{\mathrm{f}}$ are no mass terms for fermions present because only singlets under $\mathrm{SU_C}(3) \times \mathrm{SU_L}(2) \times \mathrm{U_Y}(1)$ can acquire a mass with an interaction of the type $m^2\phi^\dagger\phi$ without breaking the gauge invariance. In order to accommodate mass terms for fermions and gauge fields, electroweak symmetry breaking, leading to $\mathscr{L}_\phi$ is introduced.

The scalar doublet is introduced in the SM as

$$\phi = \frac{1}{\sqrt{2}}\begin{pmatrix} \varphi_1 + i\varphi_2 \\ \varphi_3 + i\varphi_4 \end{pmatrix}. \tag{1.6}$$

NOTE: check if I need to add constants here

Its field potential is of the form

$$V(\phi) = \mu^2\phi^\dagger\phi + \lambda(\phi^\dagger\phi)^2, \tag{1.7}$$

with $\mu^2 < 0$ and λ a positive integer. This choice of parameters gives the potential a "Mexican hat" shape. I has an infinite set of minima (ground states) and by expanding the field around an arbitrary choice of ground state, the electroweak symmetry is broken ($\not{E}\not{W}$):

$$\phi = \begin{pmatrix} 0 \\ \frac{v}{\sqrt{2}} \end{pmatrix} + \hat{\phi}, \tag{1.8}$$

where v is the vacuum expectation value (vev), measured to be around 245 GeV and corresponds to $\sqrt{\frac{-\mu}{\lambda}}$. The scalar doublet's four degrees of freedom is reduced to three degrees of freedom that couple to the gauge fields and mix with the W^+, W^- and Z bosons. The remaining fourth degree of freedom has given rise ta physically observable particle , called the Brout-Englert-Higgs (BEH) boson. This spontaneous symmetry breaking leaves the gauge invariance intact and gives masses to the $\mathrm{W}^\pm$ and Z bosons as:

$$m_{\mathrm{W}} = \frac{1}{2} v |g| \quad \text{and} \quad m_{\mathrm{Z}} = \frac{1}{2} v \sqrt{g'^2 + g^2}. \tag{1.9}$$

The Brout-Englert-Higgs field couples universally fermions with a strength proportional to their masses, and to gauge bosons with a strength proportional to the square of their masses.

1.3 Flavour changing currents in the SM

Flavour changing charged currents are introduced in 1963 by Nicola Cabibbo [8]. Via interaction with a W boson the flavour of the quarks is changed. At the time of the postulation, only up, down and strange quarks were known and the charged weak current was described as a coupling between the up quark and $\mathrm{d}_{\mathrm{weak}}$, where $\mathrm{d}_{\mathrm{weak}}$ is a linear combination of the down and strange quarks, $\mathrm{d}_{\mathrm{weak}} = \cos\theta_c \mathrm{d} + \sin\theta_c \mathrm{s}$. This linear combination is a direct consequence of the chosen rotation

$$\begin{pmatrix} \mathrm{d}_{\mathrm{weak}} \\ \mathrm{s}_{\mathrm{weak}} \end{pmatrix} = \begin{pmatrix} \cos\theta_c & \sin\theta_c \\ -\sin\theta_c & \cos\theta_c \end{pmatrix} \begin{pmatrix} \mathrm{d} \\ \mathrm{s} \end{pmatrix} = \mathscr{R} \begin{pmatrix} \mathrm{d} \\ \mathrm{s} \end{pmatrix}, \tag{1.10}$$

where the rotation angle θ_c is known as the Cabibbo angle. This provides a definition for the charged weak current between u and d quarks,

$$J_\mu = \bar{\mu} \gamma_\mu (1 + \gamma_5) \mathrm{d}_{\mathrm{weak}}. \tag{1.11}$$

A consequence of Cabibbo's approach is that the $\mathrm{s}_{\mathrm{weak}}$ is left uncoupled, leading to Glashow, Iliopoulos and Maiani (GIM) [9–11] to require the existence of a fourth quark with charge $\frac{2}{3}$. This quark, known as the charm quark, couples to $\mathrm{s}_{\mathrm{weak}}$ and a new definition of the charged weak current is modified to

$$J_\mu = \begin{pmatrix} u & c \end{pmatrix} \gamma_\mu (1 + \gamma_5) \mathscr{R} \begin{pmatrix} d \\ s \end{pmatrix} = \bar{U} \gamma_\mu (1 + \gamma_5) \mathscr{R} D. \tag{1.12}$$

The neutral weak current is defined as

$$J_3 = \bar{U} \gamma_\mu (1 + \gamma_5) \left[\mathscr{R}, \mathscr{R}^\dagger \right] D, \tag{1.13}$$

and is diagonal in flavour space. This has as consequence that no flavour changing neutral currents occur at tree-level Feynmann diagrams[2] .

NOTE: should I explain feynmann diagrams?

[2] Feynmann diagrams are physical representation of interaction between particles. They are based on Feynmann rules [1].

Kobayashi and Maskawa generalised the Cabibbo rotation matrix to accommodate for a third generation of quarks. The result is a 3×3 unitary matrix known as the CKM matrix, responsible for the mixing of weak interaction states of down-type quarks:

$$\begin{pmatrix} \mathrm{d}_{\mathrm{weak}} \\ \mathrm{s}_{\mathrm{weak}} \\ \mathrm{b}_{\mathrm{weak}} \end{pmatrix} = \begin{pmatrix} V_{\mathrm{ud}} & V_{\mathrm{us}} & V_{\mathrm{ub}} \\ V_{\mathrm{cd}} & V_{\mathrm{cs}} & V_{\mathrm{cb}} \\ V_{\mathrm{td}} & V_{\mathrm{ts}} & V_{\mathrm{tb}} \end{pmatrix} \begin{pmatrix} \mathrm{d} \\ \mathrm{s} \\ \mathrm{b} \end{pmatrix} = \mathscr{V}_{\mathrm{CKM}} \begin{pmatrix} \mathrm{d} \\ \mathrm{s} \\ \mathrm{b} \end{pmatrix}. \tag{1.14}$$

The unitarity of the matrix ($\mathscr{V}^{\dagger}_{\mathrm{CKM}} \mathscr{V}_{\mathrm{CKM}} = \mathbb{1}$). A general 3×3 unitary matrix depends on three real angles and six phases. For the CKM matrix, the freedom to redefine the phases of the quark eigenstates can remove fives of the phases, leaving a single physical phase known as the Kobayashi-Maskawa phase. This phase is responsible for the charge parity violation in the SM [12]. Each element V_{ij} of $\mathscr{V}_{\mathrm{CKM}}$ represents the transition probability of a quark i going to a quark j, and is experimentally determined to be [3]

$$\mathscr{V}_{\mathrm{CKM}} = \begin{pmatrix} 0.97425 \pm 0.00022 & 0.2253 \pm 0.0008 & (4.13 \pm 0.49)10^{-3} \\ 0.225 \pm 0.008 & 0.986 \pm 0.016 & (41.1 \pm 1.3)10^{-3} \\ (8.4 \pm 0.6)10^{-3} & (40.0 \pm 2.7)10^{-3} & 1.021 \pm 0.032 \end{pmatrix}. \tag{1.15}$$

From Equation 1.15 follows that top quarks predominantly decay via charged weak currents to bottom quarks, with a probability consistently with unity. In the SM, FCNC can only occur via higher loop Feynmann diagrams which are highly suppressed. The expected transition probabilities for a top quark decaying via a FCNC interaction in the SM are given in Table 1.4, where it is clear that the FCNC sector of the SM is still beyond the reach of the sensitivity of current experiments.

Table 1.4: The predicted branching ratios $\mathscr{B}$ for FCNC interactions involving the top quark in the SM [13]

Process	$\mathscr{B}$ in the SM	Process	$\mathscr{B}$ in the SM
$\mathrm{t} \to \mathrm{uZ}$	$8\ 10^{-17}$	$\mathrm{t} \to \mathrm{cZ}$	$1\ 10^{-14}$
$\mathrm{t} \to \mathrm{u}\gamma$	$4\ 10^{-16}$	$\mathrm{t} \to \mathrm{c}\gamma$	$5\ 10^{-14}$
$\mathrm{t} \to \mathrm{ug}$	$4\ 10^{-14}$	$\mathrm{t} \to \mathrm{cg}$	$5\ 10^{-12}$
$\mathrm{t} \to \mathrm{uH}$	$2\ 10^{-17}$	$\mathrm{t} \to \mathrm{cH}$	$3\ 10^{-15}$

1.4 Motivations for new physics

NOTE: Reread and elaborate

Many high energy experiments confirm the success of the SM. In particular the scalar boson, the cornerstone of the SM, has consecrated the theory. Unfortunately there are also strong indications that the SM ought to be a lower energy expression of a more global theory. The existence of physics beyond the SM(BSM) [14] is strongly motivated. These motivations are based on direct evidence from observation such as the existence of neutrino masses, the existence of dark matter and dark energy, or the matter-antimatter asymmetry, and also from theoretical problems such as the hierarchy problem, the coupling unification or the large numbers of free parameters in the SM.

In the SM, the neutrino is assumed to be massless, whilst experiments with solar, atmospheric, reactor and accelerator neutrinos have established that neutrinos can oscillate and change flavour during flight [15, 16]. These oscillations are only possible when neutrino's have masses. The flavour neutrinos (ν_e, ν_μ, ν_τ) are then linear expressions of the fields of at least three mass eigenstate neutrinos ν_1, ν_2, and ν_3.

The ordinary or baryonic matter described by the SM describes only 5% of the mass (energy) content of the universe. Astrophysical evidence indicated that dark matter is contributing to approximately 27%, and dark energy to 68% of the content of the universe. From the measurements of the temperature and polarizations anisotropies of the cosmic microwave background by the Planck experiment [17], the density of cold non baryonic matter is determined. Cold dark matter is assumed to be only sensitive to the weak and gravitational force, leading to only one possible SM candidate: the neutrino. However, these are too light to account for the vast amount of dark matter and other models are needed. Dark energy is assumed to be responsible for the acceleration in the expansion of the universe [18].

At the big bang matter and antimatter is assumed to be produced in equal quantities. However, it is clear that we are surrounded by matter. So where did all the antimatter go? In 1967, Sakharov identified three mechanisms that are necessary to obtain a global matter antimatter asymmetry [19]. These mechanisms are baryon and lepton number violation, at a given moment in time there was a thermal imbalance for the interactions in the universe, and there is charge C and charge parity CP violation[3]. The large numbers of free parameters in the SM are taken as nine fermion masses, three CKM mixing angles and one CP violating phase, one EM coupling constant g', one weak coupling constant g, one strong coupling constant g_s, one QCD vacuum angle, one vacuum expectation value, and one mass of the scalar boson. This large number of free parameters lead to the expectation of a more elegant, general theory beyond the SM.

The hierarchy problem [20] is related to the huge difference in energy between the weak scale and the Planck scale. The vev of the Brout-Englert-Higgs field determines the weak scale that is approximately 246 GeV. The radiative corrections to the scalar boson squared mass m_H^2, coming from its self couplings and couplings to fermions and gauge bosons, are quadratically proportional to the ultraviolet momentum cut-off Λ_UV. This cut-off is at least equal to the energy to which the SM is valid without the need of new physics. The SM is valid up to the Planck mass making the correction to m_H^2 about thirty orders of magnitude larger than m_H^2. This implies that an extraordinary cancellation of terms should happen. This is also known as the naturalness problem of the H boson mass.

The correction to the squared mass of the scalar boson coming from a fermion f, coupling to the scalar field ϕ with a coupling λ_f is given by

$$\Delta m_\mathrm{H}^2 = -\frac{|\lambda_\mathrm{f}|^2}{8\pi^2}\Lambda_\mathrm{UV}^2, \tag{1.16}$$

[3] The rate of a process $i \to f$ can be different from the CP-conjugate process: $\tilde{i} \to \tilde{f}$. The SM includes sources of CP-violation through the residual phase of the CKM matrix. However, these could not account for the magnitude of the asymmetry observed.

while the correction to the mass from a scalar particle S with a mass m_{S}, coupling to the scalar field with a Lagrangian term $-\lambda_{mathrmS}|\phi|^2|\mathrm{S}|^2$ is

$$\Delta m_{\mathrm{H}}^2 = -\frac{|\lambda_{\mathrm{S}}|^2}{16\pi^2}\left(\Lambda_{\mathrm{UV}}^2 - 2m_{\mathrm{S}}^2 \ln\left(\frac{\Lambda_{\mathrm{UV}}}{m_{\mathrm{S}}}\right) + \ldots\right). \tag{1.17}$$

As one can see the correction term to m_{H}^2 is much larger than m_{H}^2 itself. By introducing BSM physic models that introduce new scalar particles at TeV scale that couple to the scalar boson can cancels the Λ_{UV}^2 divergence and avoid this fine-tuning.

Also the large mass differences between the fermions related to the Yukawa couplings can go up to six order of magnitude in the case of the electron and the top quark and constitute the fermion mass hierarchy problem.

The choice of the $\mathrm{SU_C}(3) \times \mathrm{SU_L}(2) \times \mathrm{U_Y}(1)$ symmetry group itself as well as the separate treatment of the three forces included in the SM raises concern. The intensity of the forces show a large disparity around the electroweak scale, but have comparable strengths at higher energies. The electromagnetic and weak forces are unified in a electroweak interaction, but the strong coupling constant does not encounter the other coupling constants at high energies. In order to reach a grand unification, the running of couplings can be modified by the addition of new particles in BSM models.

1.5 An effective approach beyond the SM: FCNC involving a top quark

The closeness of the top mass to the electroweak scale led physicist to believe that it is a sensitive probe for new physics. Its property study is therefore an important topic of the experimental program at the LHC. Several extensions of the SM enhance the FCNC branching ratios and can be probed at the LHC [13], from which some of them are shown in Table 1.5. Previous searches have been performed at the Fermilab Tevatron by the CDF [21] and D0 [22] collaborations, and at the LHC by the ATLAS [23–26] and CMS [27–31] collaborations.

NOTE: check with references from TOP2017

Table 1.5: The predicted branching ratios $\mathcal{B}$ for FCNC interactions involving the top quark in some BSM models [13]: quark singlet (QS), generic two Higgs doublet model (2HDM) and the minimal super symmetric extensions to the SM (MSSM);

Process	QS	2HDM	MSSM	Process	QS	2HDM	MSSM
$\mathrm{t} \to \mathrm{uZ}$	$\leq 1.1\ 10^{-4}$	–	$\leq 2\ 10^{-6}$	$\mathrm{t} \to \mathrm{cZ}$	$\leq 1.1\ 10^{-4}$	$\leq 10^{-7}$	$\leq 2\ 10^{-6}$
$\mathrm{t} \to \mathrm{u}\gamma$	$\leq 7.5\ 10^{-9}$	–	$\leq 2\ 10^{-6}$	$\mathrm{t} \to \mathrm{c}\gamma$	$\leq 7.5\ 10^{-9}$	$\leq 10^{-6}$	$\leq 2\ 10^{-6}$
$\mathrm{t} \to \mathrm{ug}$	$\leq 1.5\ 10^{-7}$	–	$\leq 8\ 10^{-5}$	$\mathrm{t} \to \mathrm{cg}$	$\leq 1.5\ 10^{-7}$	$\leq 10^{-4}$	$\leq 8\ 10^{-5}$
$\mathrm{t} \to \mathrm{uH}$	$\leq 4.1\ 10^{-5}$	$\leq 5.5\ 10^{-6}$	$\leq 10^{-5}$	$\mathrm{t} \to \mathrm{cH}$	$\leq 4.1\ 10^{-5}$	$\leq 10^{-3}$	$\leq 10^{-5}$

The impact of BSM models can written in a model independent way by means of an effective field theory valid up to an energy scale Λ. The leading effects are parametrized by a set of fully gauge symmetric dimension-6 operators that are added to the SM Lagrangian and can be reduced to a minimal set of operators as discussed in [32, 33]. The full Lagrangian, neglecting neutrino physics, in the fully gauge symmetric case is given by

$$\mathscr{L}_{\mathrm{SM+EFT}} = \mathscr{L}_{\mathrm{SM}} + \sum_{\mathrm{i}} \frac{\bar{c}_{\mathrm{i}}}{\Lambda^2}\mathscr{O}_{\mathrm{i}} + \mathscr{O}\left(\frac{1}{\Lambda^3}\right), \tag{1.18}$$

where the Wilson coefficients $\bar{c}_{\mathrm{i}}$ depend on the considered theory and on the way that new physics couples to the SM particles. Considering that Λ is large, contributions suppressed by powers of Λ greater than two are neglected. Moreover, all four fermion operators are omitted for the rest of this thesis. After electroweak symmetry breaking the operators induce [13, 34] both corrections to the SM couplings and new interactions at tree level such as FCNC interactions. The FCNC interactions of the top quark that are not present in the SM are given by

$$\begin{aligned}
\mathscr{L}^{\mathrm{t}}_{\mathrm{EFT}} = \frac{\sqrt{2}}{2}\sum_{\mathrm{q=u,c}} \Bigg[& g'\frac{\kappa_{\mathrm{t}\gamma\mathrm{q}}}{\Lambda}\mathrm{A}_{\mu\nu}\bar{\mathrm{t}}\sigma^{\mu\nu}\left(f^{\mathrm{L}}_{\gamma\mathrm{q}}P_{\mathrm{L}} + f^{\mathrm{R}}_{\gamma\mathrm{q}}P_{\mathrm{R}}\right)\mathrm{q} && (1.19)\\
& + \frac{g}{2\cos\theta_{\mathrm{W}}}\frac{\kappa_{\mathrm{tZq}}}{\Lambda}\mathrm{Z}_{\mu\nu}\bar{\mathrm{t}}\sigma^{\mu\nu}\left(f^{\mathrm{L}}_{\mathrm{Zq}}P_{\mathrm{L}} + f^{\mathrm{R}}_{\mathrm{Zq}}P_{\mathrm{R}}\right)\mathrm{q} && (1.20)\\
& + \frac{\sqrt{2}}{4\cos\theta_{\mathrm{W}}}\zeta_{\mathrm{tZq}}\bar{\mathrm{t}}\gamma^{\mu}\left(\tilde{f}^{\mathrm{L}}_{\mathrm{q}}P_{\mathrm{L}} + \tilde{f}^{\mathrm{R}}_{\mathrm{q}}P_{\mathrm{R}}\right)\mathrm{q}\mathrm{Z}_{\mu} && (1.21)\\
& + g_{\mathrm{S}}\frac{\kappa_{\mathrm{gqt}}}{\Lambda}\mathrm{Z}_{\mu\nu}\bar{\mathrm{t}}\sigma^{\mu\nu}\left(f^{\mathrm{L}}_{\mathrm{gq}}P_{\mathrm{L}} + f^{\mathrm{R}}_{\mathrm{gq}}P_{\mathrm{R}}\right)\mathrm{q}\mathrm{G}^{\mathrm{a}}_{\mu\nu} && (1.22)\\
& + \eta_{\mathrm{Hqt}}\bar{\mathrm{t}}\left(\hat{f}^{\mathrm{L}}_{\mathrm{q}}P_{\mathrm{L}} + \hat{f}^{\mathrm{R}}_{\mathrm{q}}P_{\mathrm{R}}\right)\mathrm{qH} + \mathrm{h.c.}\Bigg], && (1.23)
\end{aligned}$$

where the the value of the FCNC couplings at scale Λ are represented by κ_{tZq},κ_{gqt},$\kappa_{\mathrm{t}\gamma\mathrm{q}}$,$\zeta_{\mathrm{tZq}}$, and η_{Hqt}. These are assumed to be real and positive, with the unit of GeV^{-1} for $\kappa_{\mathrm{tXq}}/\Lambda$ and no unit for ζ_{xqt} and η_{xqt}. In the equation $\sigma^{\mu\nu}$ equals to $\frac{i}{2}\left[\gamma^{\mu},\gamma^{\nu}\right]$, and the left- and right-handed chirality projector operators are denoted by P_{L} and P_{R}. The electromagnetic coupling constant is denoted by g', the strong interaction coupling is denoted as g_{s}, while the electroweak interaction is parametrised by the coupling constant g and the electroweak mixing angle θ_{W}. The complex chiral parameters are normalized according to $|f^{\mathrm{L}}_{\mathrm{xq}}|^2 + |f^{\mathrm{R}}_{\mathrm{xq}}|^2 = 1$, $|\tilde{f}^{\mathrm{L}}_{\mathrm{q}}|^2 + |\tilde{f}^{\mathrm{R}}_{\mathrm{q}}|^2 = 1$, and $|\hat{f}^{\mathrm{L}}_{\mathrm{q}}|^2 + |\hat{f}^{\mathrm{R}}_{\mathrm{q}}|^2 = 1$. In the expression for $\mathscr{L}^{\mathrm{t}}_{\mathrm{EFT}}$, the unitary gauge is adopted on the scalar field is expanded around its vacuum expectation value with H being the SM scalar boson, and the field strength tensors of the photon A_{μ}, the gluon field $\mathrm{G}^{1\ldots8}_{\mu}$, and the Z boson Z^{0}_{μ} are defined as

$$\mathrm{A}_{\mu\nu} = \partial_{\mu}\mathrm{A}_{\nu} - \partial_{\nu}\mathrm{A}_{\mu},\ \mathrm{Z}_{\mu\nu} = \partial_{\mu}\mathrm{Z}_{\nu} - \partial_{\nu}\mathrm{Z}_{\mu},\ \text{and } \mathrm{G}_{\mu\nu} = \partial_{\mu}\mathrm{G}^{\mathrm{a}}_{\nu} - \partial_{\nu}\mathrm{G}^{\mathrm{a}}_{\mu} + g_{\mathrm{S}}f^{\mathrm{a}}_{\mathrm{bc}}\mathrm{G}^{\mathrm{b}}_{\mu}\mathrm{G}^{\mathrm{c}}_{\nu}. \tag{1.24}$$

Denoting the structure constant of the $\mathrm{SU_C}(3)$ group as $f^{\mathrm{a}}_{\mathrm{bc}}$. Note that there are two coupling constants arising in $\mathscr{L}^{\mathrm{t}}_{\mathrm{EFT}}$, which is a residue of electroweak symmetry breaking. The massive Z boson will appear in both the Z^{0}_{μ} field as well as the covariant derivative, leading to an extra Z-vertex.

1.6 Experimental constraints on top-FCNC

Experiments commonly put limits on the branching ratio's which allow an easier interpretation across different EFT models as

$$\mathscr{B}(\mathrm{t} \to \mathrm{qX}) = \frac{\delta^2_{\mathrm{tXq}} \Gamma_{\mathrm{t}\to\mathrm{qX}}}{\Gamma_{\mathrm{t}}}, \tag{1.25}$$

where $\Gamma_{\mathrm{t}\to\mathrm{qX}}$ represents the FCNC decay width[4] for a coupling strength $\delta^2_{\mathrm{tXq}} = 1$, and Γ_{t} the full decay width of the top quark. In the SM, supposing a top quark mass of 172.5 GeV, the full width becomes $\Gamma^{\mathrm{SM}}_{\mathrm{t}} = 1.32$ GeV [35].

Searches for top-FCNC usually adopt a search strategy depending on the experimental set-up and the FCNC interaction of interest, looking either for FCNC interactions in the production of a single top quark or in its decay for top pair interactions. In Figure 1.1, these two cases are shown for the tZq vertex.

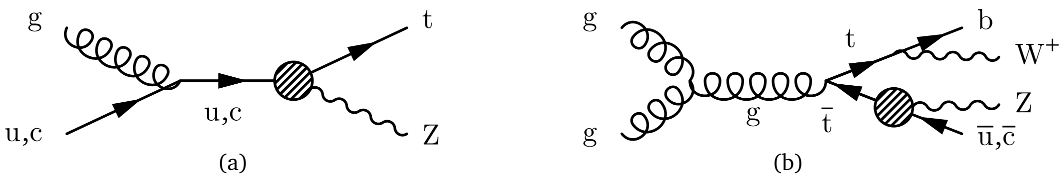

Figure 1.1: Feynman diagrams for the tZq FCNC interaction, where the FCNC interaction is indicated with the shaded dot. (a) Single top production through an FCNC interaction. (b) Top pair production with an FCNC induced decay.

The observation of top-FCNC interactions has yet to come and experiments have so far only been able to put upper bounds on the branching ratios. An overview of the best current limits is given in Table 1.6 . In Figure 1.2 a comparison is shown between the current best limits set by ATLAS and CMS with respect to several BSM model benchmark predictions. From there one can see that FCNC searches involving a Z or H boson are close to excluding or confirming several BSM theories.

NOTE: Check atlas result for tZq from top2017 proceedings when they appear

[4] The decay width of a certain process represents the probability per unit time that a particle will decay. The total decay width, defined as all possible decay widths of a particle, is inversely proportional to its lifetime.

Table 1.6: Overview of the most stringent observed and expected experimental limits on top-FCNC branching ratios $\mathscr{B}$ at 95% confidence level.

Process	Search mode	Observed $\mathscr{B}$	Expected $\mathscr{B}$	Experiment	
$t \to uZ$	top pair decay and single top production	$2.2\ 10^{-4}$	$2.7\ 10^{-4}$	CMS	[27]
$t \to u\gamma$	single top production	$1.3\ 10^{-4}$	$1.9\ 10^{-4}$	CMS	[29]
$t \to ug$	single top production	$4.0\ 10^{-5}$	$3.5\ 10^{-5}$	ATLAS	[24]
$t \to uH$	top pair decay	$2.4\ 10^{-3}$	$1.7\ 10^{-3}$	ATLAS	[26]
$t \to cZ$	top pair decay and single top production	$4.9\ 10^{-4}$	$12\ 10^{-4}$	CMS	[27]
$t \to c\gamma$	single top production	$2.0\ 10^{-3}$	$1.7\ 10^{-3}$	CMS	[29]
$t \to cg$	single top production	$2.0\ 10^{-4}$	$1.8\ 10^{-4}$	ATLAS	[24]
$t \to cH$	top pair decay	$2.2\ 10^{-3}$	$1.6\ 10^{-3}$	CMS	[26]

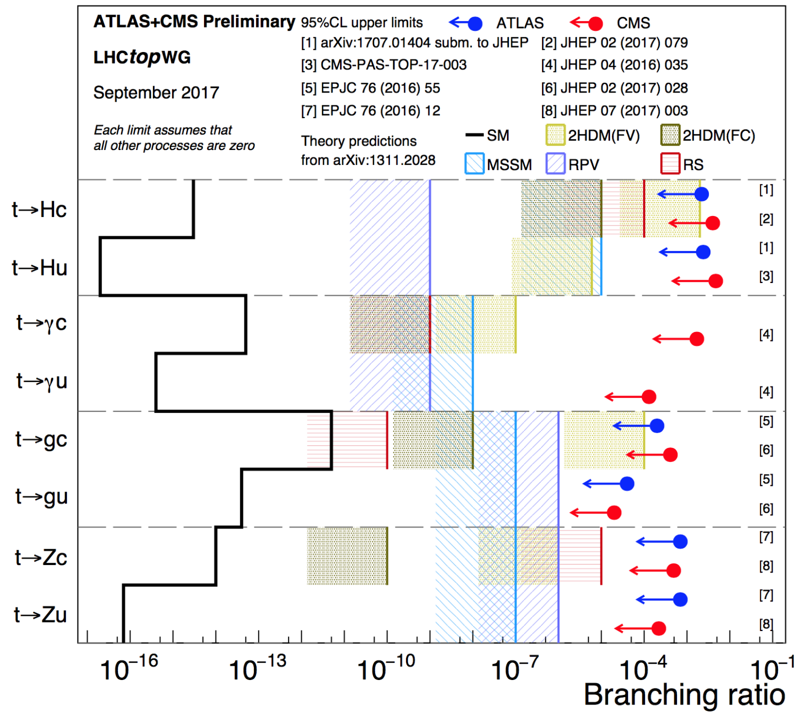

Figure 1.2: Current best limits set by CMS and ATLAS for top-FCNC interactions.

2 Experimental set-up

The main objective of the Large Hadron Collider (LHC) was the search for the Brout-Englert-Higgs boson (or scalar boson). It was known from the Linear Electron Positron(LEP)[36] and Tevatron[37] experiments that the scalar boson mass had to be larger than 114 GeV[38, 39], and smaller than around 1 TeV due to unitarity and perturbativity constraints [40]. On top of this, the search of supersymmetry or dark matter were part of the motivation for building the LHC. Since the start of its operation, the LHC is pushing the boundaries of the Standard Model, putting the best limits on physics beyond the Standard Model as well as precision measurements of the parameters of the Standard Model. One such an accomplishment is the discovery the scalar boson in 2012 by the two largest experiments at the LHC [6, 7].

In the first part of this chapter, the LHC and the acceleration process for protons to reach their design energies is discussed. The second part presents the Compact Muon Solenoid.

2.1 The Large Hadron Collider

The LHC has started its era of cutting edge science on 10 September 2008 [41] after approval by the European Organisation of Nuclear Research (CERN) in 1995 [42]. Installed in the previous Large Electron Positron collider (LEP) tunnels, the LHC consists of a 26.7 km ring, that is installed between 45 and 170 m under the French-Swiss border between Cessy (France) and Meyrin (Switzerland). Built to study rare physics phenomena at high energies, the LHC has the possibility to accelerate two type of particles - protons or ions Pb^{45+} - and provides collisions at four points of interaction or bunch crossings.. At the interaction points, experiments are installed in order to study the collisions.

As can be seen in Figure 2.1, the LHC is last element in a chain of creation, injection and acceleration of protons. Protons are obtained by ionising hydrogen and injected in a linear accelerator (LINAC 2), where they obtain an energy of 50 MeV. They continue to the proton synchrotron booster (PSB or Booster), where the proton packets are accelerated to 1.4 GeV and are split up in twelve. The proton synchrotron (PS) increases their energy to 25 GeV before handing the protons to the super proton synchrotron (SPS), where the proton reach an energy of 450 GeV. Each accelerator ring increases in radius in order to reduce the energy loss of the protons by synchrotron radiation. This energy loss is proportional to the fourth power of the proton energy and inversely proportional to the bending radius. The protons are then injected into opposite directions into the LHC, where they are accelerated to 3.5 TeV (in 2010 and 2011), 4 TeV (in 2012 and 2013) or 6.5 TeV (in 2015 and 2016) [43]. Before the start up of the LHC in 2010, the previous energy record was held by the Tevatron collider at Fermilab, colliding proton with antiprotons at $\sqrt{s} = 1.96$ TeV.

The beam has a bunch structure obtained by the injection scheme and properties of the dump system. These bunches are obtained in the PS with 25 ns spacing for run II. The operation of accelerating and transferring to the LHC is repeated 12 times for each counter-rotating beam. When completely filled, the LHC nominally contains 2220 bunches in run II, compared to 1380 in run I (design: 2200). At full intensity, it would have nearly 2800 bunches but this is limited due to SPS.

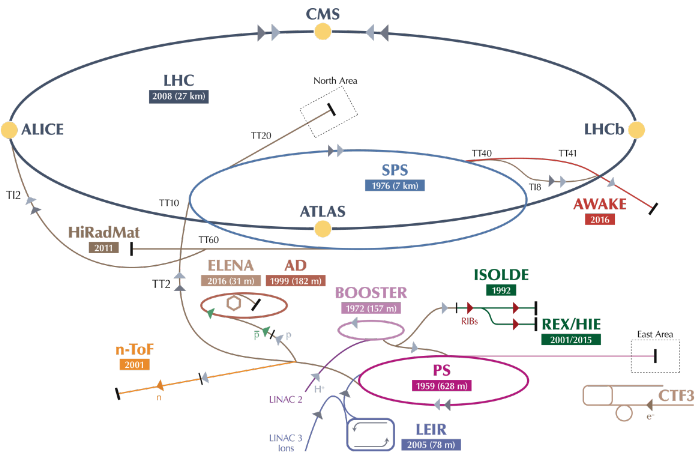

Figure 2.1: Schematic representation of the accelerator complex at CERN [44]. The LHC (dark blue) is the last element in chain of accelerators. Protons are successively accelerated by LINAC 2, the Booster, the Proton Synchrotron (PS) and the Super Proton Synchrotron (SPS) before entering the LHC.

The LHC is home to seven experiments that are placed on an interaction point:

- A Toroidal LHC ApparatuS (ATLAS [45]) and the Compact Muon Solenoid (CMS [46]) experiments are the two general purpose detectors at the LHC. They both have a hermetic, cylindrical structure and were designed to search for new physics phenomena as well as precision measurements of the Standard Model. The existence of two distinct experiments allows cross-confirmation for any discovery.
- A Large Ion Collider Experiment (ALICE [47]) and the LHC Beauty (LHCb [48]) experiments are focusing on specific phenomena. ALICE studies strongly interacting matter at extreme energy densities where quark-gluon plasma forms from heavy ions (Pb-Pb or p-Pb). LHCb searches for differences between matter and anti matter by means of the b quark, while focussing on CP symmetry violation.
- The forward LHC (LHCf [49]) and the TOTal cross section, Elastic scattering and diffraction dissociation Measurement (TOTEM [50]) experiments are two smaller experiments that

focus on interactions where protons or heavy ions only meet while head on collisions take place. LHCf consists of two parts placed before and after ATLAS and studies particles created at very small angles. TOTEM is placed in the same cavern as CMS and performs precise measurements of the LHC luminosity.

- The Monopoles and Exotics Detector At the LHC (MoEDAL [51]) experiment is situated near LHCb and tries to find magnetic monopoles.

2.1.1 LHC design and operation

The most important quantity at the LHC is the luminosity[52]. This is a measurement of the number of collisions that can be produced in a detector per m^2 and per second. The LHC collisions create a number of events per second given by

$$N_{event} = L\sigma_{event}, \tag{2.1}$$

where σ_{event} is the cross section of the event of interest and L the machine luminosity. This luminosity depends only on the beam parameters and is for a Gaussian beam expressed as

$$L = \frac{1}{4\pi} N_b n_b f_{rev} \frac{N_b}{\epsilon_n} \left(1 + \left(\frac{\theta_c \sigma_z}{2\sigma^*}\right)^2\right)^{\frac{-1}{2}} \frac{\gamma_r}{\beta^*}. \tag{2.2}$$

The number of particles per bunch is expressed by N_b, while n_b is the number of bunches per beam, f_{rev} the revolution frequency, γ_r the relativistic gamma factor, ϵ_n the normalized transverse beam emittance - a quality for the confinement of the beam , β^* the beta function at the collision point - a measurement for the width of the beam, θ_c the angle between the two beams at the interaction point, σ_z the mean lengths of one packet, and σ^* the mean height of one packet. In Equation 2.2), the blue part represents the stream of particles, the red represents the brilliance; and the green part represents the geometric reduction factor due to the crossing angle at the interaction point. Hence, in order to enhance the chances for exploration of rare events and thus enhancing the number of collisions. High beam energies as well as high beam intensities are required.

The peak design luminosity for the LHC in 2016 was 10^{34} $1/(m^2 s)$, which leads to about 1 billion proton interactions per second. In 2016, the LHC was around 10% above this design luminosity[53]. This luminosity is not a constant in time. It diminishes due to collisions between the beams, and the interaction of the protons and the particle gas that is trapped in the centre of the vacuum tubes due to the magnetic field. The intern diffusion of the beam degrades the emittance and therefore also the luminosity. For this reason, the mean lifetime of a beam inside the LHC is around 15 h. The integrated luminosity - the luminosity provided for a certain time range - recorded by CMS and ATLAS over the year 2016 is given in Figure 2.1.1. In Run II, the peak luminosity is 13-17 10^{33} $1/(cm^2 s)$ compared to 7.7 10^{33} $1/(cm^2 s)$ in Run I.

Inside the LHC ring [54], the protons are accelerated by the means of radio frequency cavities, while 1232 magnets of approximately 15 m long, weighing 35 t ensure the deflection of the beams. The cross section view of such a dipole is given in Figure 2.4. The two proton beams circulate in opposite direction in separate pipes inside of the magnet. Through the use of a strong

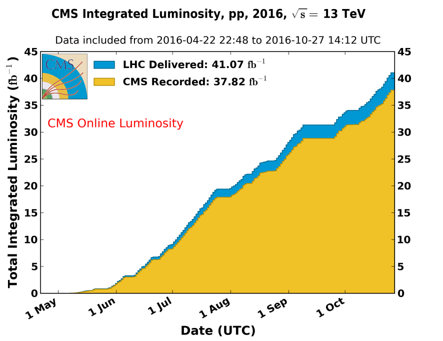

Figure 2.2: Cumulative luminosity measured online versus day delivered to (blue), and recorded by CMS (orange) during stable beams and for proton collisions at 13 TeV centre-of-mass energy in 2016. The delivered luminosity accounts for the luminosity delivered from the start of stable beams until the LHC requests CMS to turn off the sensitive detectors to allow a beam dump or beam studies.

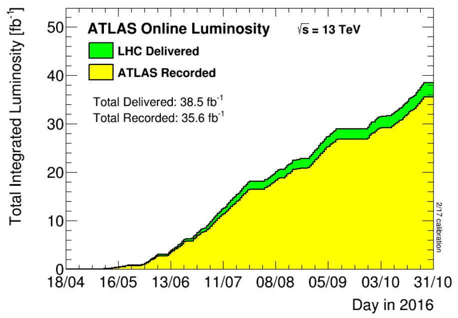

Figure 2.3: Total Integrated Luminosity in 2016 Cumulative luminosity versus time delivered to (green) and recorded by ATLAS (yellow) during stable beams for proton collisions in 2016. The delivered luminosity accounts for luminosity delivered from the start of stable beams until the LHC requests ATLAS to put the detector in a safe standby mode to allow for a beam dump or beam studies. Shown is the luminosity as determined from counting rates measured by the luminosity detectors.)

electric current in the coils around the beam pipe, magnetic fields are generated and cause the protons to bend in the required orbits. In order to get the coil to become superconducting and able to produce - with the aid of an iron return yoke - a strong magnetic field of 8.3 T, the magnet structure is surrounded by a vessel. This vessel is filled with liquid Helium making it possible to cool down the magnet to 1.9 K. In order to get more focussed and stabilised proton beam, other higher-order multipole and corrector magnets are placed along the LHC tunnel.

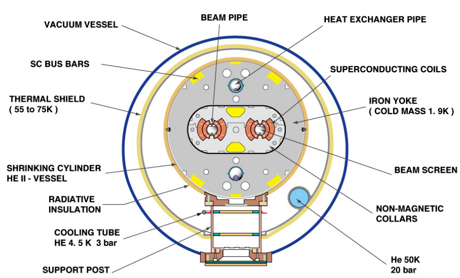

Figure 2.4: Schematic representation of the LHC dipole [55] . Two beam pipes where the proton beams circulate around the LHC ring are shown. The superconducting coils generate a magnetic field of 8.3 Tthat steer the protons in the circular path.

2.2 The Compact Muon Solenoid

At one of the collision points of the LHC, the CMS detector[56–58] is placed. Weighing 14 000 t, This cylindrical detector is about 28.7 m long and 15 m in diameter, weighing around 14 000 t. It has an onion like structure of several specialised detectors and contains a superconducting solenoid with a magnetic field of 3.8 T. The CMS detector is designed in a way that it can address the needs of physics coming from the LHC. Living in a hadronic environment, multi-jet processes produced by the strong interaction are a main source of background for rare physics processes. Therefore, good identification, momentum resolution, and charge determination of muon, electrons and photons is one of the main goals of the CMS detector. Further it provides a good charged particle momentum resolution and reconstruction efficiency in the inner tracker such that for example jets coming from b quarks or tau particles can be identified. Also the electromagnetic resolution for an efficient photon and lepton isolation as well as a good hadronic calorimeter for the missing transverse energy were kept into account while designing CMS. In Figure 2.5, an overview of the CMS detector is given.

The LHC provides many collisions in a short amount of time. In order to discriminate between consecutive collisions - known as out of time pile up events - , CMS has to complete the full data acquisition for one collision event before the next one happens (around 25 ns in Run II and around 50 ns in Run I [59]). Furthermore, since the photons are in packets, around 21 in Run I and approximately 40 in Run II inelastic collisions happen every beam crossing . This creates a great amount of background processes in the detector called in time pile up events. Due to this difficult conditions, the detector has a high granularity which on its turn creates a need for huge number of synchronized electronic channels. Furthermore, due to to high flux of particles in the regions close to the beam, the electronics have to be able to endure high radiation.

Before the start of taking collision data for 13 TeV operations on 3 June, CMS had a long shutdown (LS1)[61]. During this shut down several upgrades were performed. The innermost part of detection material in CMS (pixel) is made of three concentric cylindrical layers in run I. At the end of 2016 it is upgraded by adding a fourth layer, enhancing the particle tracking capabilities of CMS. In order to be able to incorporate this new layer, the section of the beryllium beam pipe within CMS was replaced by a narrower one during LS1. For this, the pixel was removed and reinserted into CMS. In order to avoid long damage caused by the intense particle flux at the heart of CMS, the tracker is been made ready to operate at much lower temperature than before. During Run I, a small problem was detected in the electromagnetic calorimeter preshower system. For this, the preshower discs were removed, repaired and reinstalled successfully inside CMS in 2014. To help the discrimination between interesting low momentum muons coming from collisions and muons caused by backgrounds, a fourth triggering and measurement station for muons was added in each of the end caps. CMS measures the collision rate within the detector and monitors beam related backgrounds. For this, several new detectors were installed into CMS during LS1.

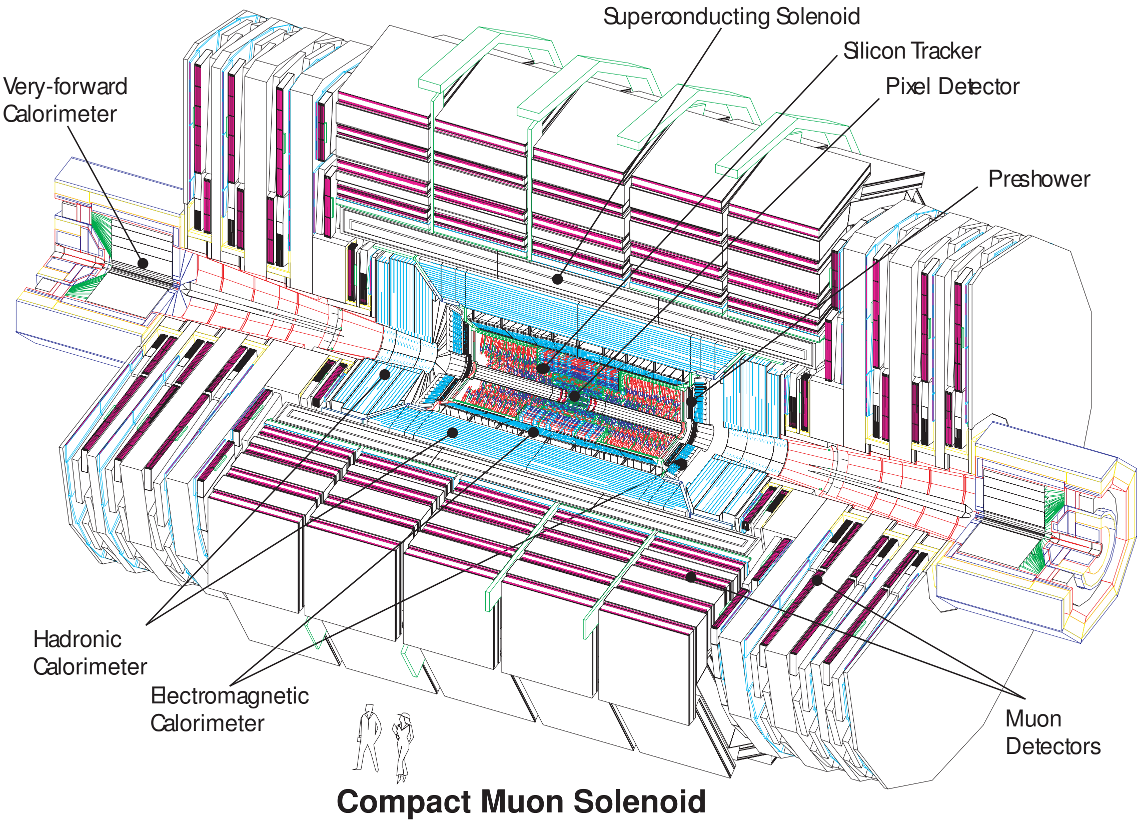

Figure 2.5: Mechanical layout of the CMS detector[60].

2.2.1 CMS coordinate system

The coordinate system used by CMS can be found in Figure 2.6. The origin of the right handed orthogonal coordinate system is chosen to be the point of collisions. The x-axis points towards the centre of the LHC ring such that the y-axis points towards the sky, and the z-axis lies tangent to the beam axis. Since the experiment has a cylindrical shape, customary coordinates are used to describe the momentum $\vec{p}$: the distance ρ, the azimuthal angle $\phi \in [-\pi, \pi]$ - the angle between the x-axis and the projection in the transverse plane of $\vec{p}$ ($\vec{p}_T$) - , the pseudo-rapidity η - expressed by the polar angle θ between the direction of $\vec{p}$ and the beam - :

$$\eta = -\ln\left(\tan\left(\frac{\theta}{2}\right)\right). \tag{2.3}$$

For the energies considered at the LHC, where $E >> m$, the pseudo-rapidity is a good approximation of the rapidity y

$$y = \frac{1}{2}\ln\left(\frac{E+p_z}{E-p_z}\right), \tag{2.4}$$

where the difference of rapidities of two particles is invariant under a Lorentz boost in the z-direction.

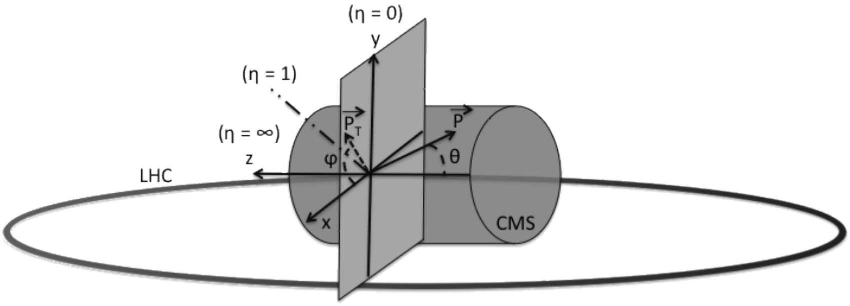

Figure 2.6: Representation of the coordinate system used by CMS. The point of origin is put at the collision point. The x-axis points towards the centre of the LHC ring such that the z-axis lies tangent to the beam axis.

2.2.2 Towards the heart of CMS

The CMS detector consists of two parts; a central barrel around the beam pipe ($|\eta| < 1.4$) and two plugs to ensure the hermeticity of the detector. In Figure 2.5 and Figure 2.7 the onion like structure of the CMS detector is visible. The choice of a solenoid of 12.9 m long and 5.9 m diameter gives the advantage of bending the particle trajectories in the transverse plane. The hadronic calorimeter, the electromagnetic calorimeter and the tracker are within the solenoid, while the muon chambers are placed outside the solenoid.

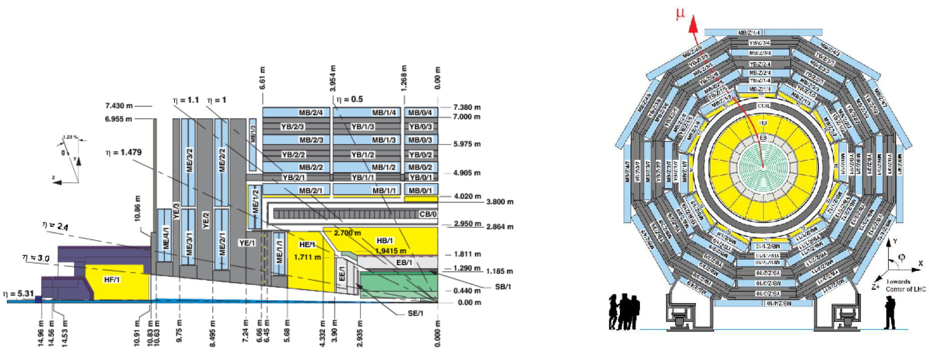

Figure 2.7: Schematic view of the CMS detector in the Run I configuration. (LEFT) Longitudinal view of one quarter of the detector. (RIGHT) Transversal view of one quarter of the detector. The muon system barrel elements are denoted as MBZ/N/S, where z= −2... + 2 is the barrel wheel number, n= 1...4 the station number and S= 1...12 the sector number. Similary, the steel return yokes are denoted as YBZ/N/S. The solenoid is denoted as CB0, while the hadronic calorimeter is denoted as HE (end cap)/ HB (barrel)/HF(forward) and the electromagnet calorimeter as EE(end cap)/EB (barrel). The green part represents the tracking system[62]

.

2.2.2.1 Muon system

The outermost part of CMS consists of the muon system. The magnet return yoke is interleaved with gaseous detector chambers for muon identification and momentum measurement. The barrel contains muon stations arranged in five separate iron wheels, while in the end cap four muon stations are mounted onto three independent iron discs on each side. Each barrel wheel has 12 sectors in the azimuthal angle.

The muon system is divided into three parts, shown in Figure 2.8[62]. The muon rate and neutron induced backgrounds are small and the magnetic field is very low for the barrel, thus CMS can use drift tube (DT) chambers. For the end caps however, the muon and background flux is much higher and there is a need to use cathode strip chambers (CSC) which are able to provide a faster response, higher granularity and have a better resistance against radiation. In order to form a redundant trigger system, resistive plate chambers (RPC) are added. This makes a total of 250 DT chambers, 540 CSC and 610 RPC. In Figure 2.7 the arrangement is shown.

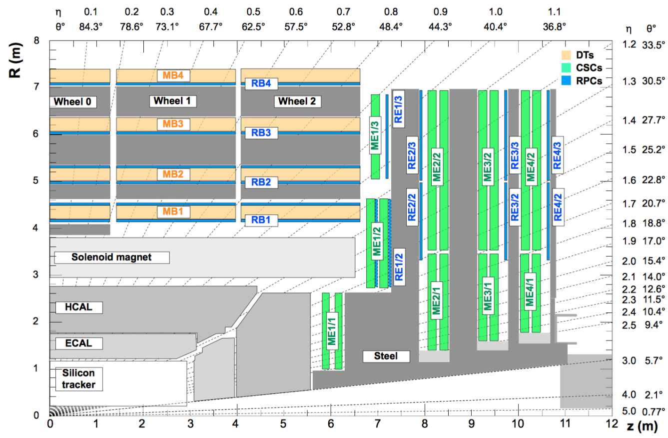

Figure 2.8: Schematic view of one quarter of the CMS muon system in the Run I configuration. [62]

Providing a measurement for $|\eta| < 1.2$. The DT chambers in the barrel are on average 2×2.5 m in size and consist of 12 layers of DT cells - 4 cm wide gas tubes with positively charged stretched wire inside - arranged in three groups of four. The $r\phi$ coordinate is provided by the two outside groups, while the middle group measures the z coordinate. For each ϕ sector, the DT chamber is mixed with the flux return yoke. For the outer muon station, the DT chamber contains only 8 layers of DT cells, providing a muon position in th $r\phi$ plane. There are four CSC stations in each end cap, providing muon measurements for $0.9 < |\eta| < 2.4$ (Run I configuration). These CSC are multi-wired proportional chambers that consist of 6 anode wire planes crossed by 7 copper strips cathode panels in a gas volume. The r coordinate is provided by the copper strips, while ϕ coordinate comes from the anode wires, giving a two dimensional position measurement. There are six layers of RPC in the barrel muon system and one layer into each of the first three stations of the end cap. They are made from two high resistive plastic plates with an applied voltage and separated by a gas volume. Read out strips mounted on top of the plastic plates detect the signal generated by a muon passing through the gas volume. The RPC provides a fast response with a time resolution of 1 ns and covers a range of $|\eta| < 1.8$ (Run I configuration).

During the LS1, the muon system underwent major upgrades [63, 64]. In the fourth station of each end cap, the outermost rings of CSC and RPC chambers were completed, providing an angular region of $1.2 < |\eta| < 1.8$ for Run II, increasing the system redundancy, and allowing tighter cuts on the trigger quality. In order te reduce the environmental noise, outer yoke discs have been placed on both sides for the end caps. At the innermost rings of the first station, the CSC has been upgraded by refurbishing the readout electronics to make use of the full detector granularity instead of groups of three (Run I).

The muon system provides triggering on muons, identifying muons and improves the momentum measurement and charge determination of high p_T muons. On top of the muon system, the muon energy is deposited in the electromagnetic calorimeter, the hadronic calorimeter, and outer calorimeter. The high magnetic field enables an efficient first level trigger and allows a good momentum resolution of $\Delta p/p \approx 1\%$ for a p_T of 100 GeV and $\approx 10\%$ for a p_T of 1 TeV (FIXME). There is an efficient muon measurement up to $|\eta| < 2.4$.

Muon reconstruction

The muon reconstruction[65] has three subdivision: local reconstruction, regional reconstruction and global reconstruction. The local reconstruction is performed on individual detector elements such as strip and pixel hits in the inner tracking system, and muon hits and/or segments on the muon chambers. Independent tracks are reconstructed in the inner tracker - called tracker track - and in the muon system, called standalone tracks. Based on these tracks, two reconstructions are considered. The outside-in approach is referred to as Global Muon reconstruction. For each standalone track, a tracker track is found by comparing the parameters of the two tracks propagated onto a common surface. Combining the hits from the tracker track and the standalone track, gives a fit via the Kalman filter technique [66, 67] for a global muon track. The second approach is an inside-out reconstruction, creating tracker muons. All candidate tracker tracks are extrapolated to the muon system taking into account the magnetic field, the average expected energy losses, and multiple Coulomb scattering in the detector material. When at least one muon segment - DT or CSC hits - matches the extrapolated track, the corresponding tracker track is indicated as a tracker muon.

For low transverse momenta ($p_T \lesssim 5$ GeV), the tracker muon reconstruction is more efficient than the global muon approach. This is due to the fact that tracker muons only require a single muon segment in muon system, while the global muon approach requires typically segments in at least two muon stations. The global muon approach typically improves the tracker reconstruction for $p_T \gtrsim 200$ GeV.

2.2.2.2 Solenoid

Making use of the knowledge of previous experiments of ALEPH and DELPHI at LEP and H1 at HERA, CMS choose for a large super conducting solenoid with a a length of 12.9 m and a inner bore of 5.9 m[58]. With 2 168 turns, a current of 19.5 kA and a total energy of 2.7 GJ, a large bending power can be obtained for a modestly-sized solenoid. In order to ensure a good momentum resolution in the forward regions, a favourable length/radius was necessary. In Figure 2.9, a photo of the CMS solenoid is given.

The solenoid uses a high-purity aluminium stabilised conductor with indirect cooling from liquid helium, together with fully epoxy impregnation. A four-layer winding is implemented that can withstand an outward pressure of 64 atm. The NbTi cable is co-extruded by pure aluminium that acts as a thermal stabilizer and has an aluminium alloy for mechanical reinforcement. The return of the magnetic field is done by fives wheels, noted by YB in Figure 2.7.

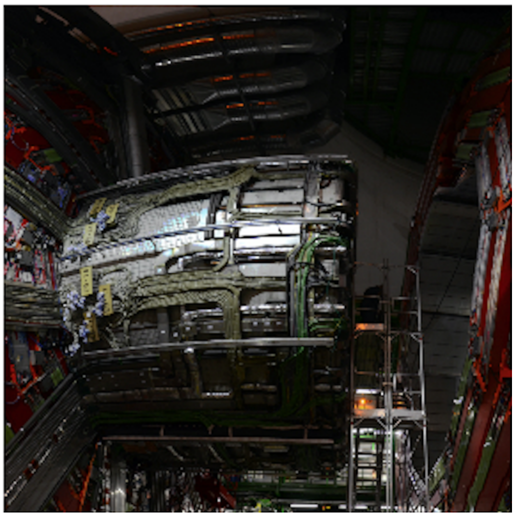

Figure 2.9: CMS solenoid during the long shutdown in 2013.

2.2.2.3 Hadronic calorimeter

The hadronic calorimeter (HCAL) is dedicated to precisely measure the energy of charged and neutral hadrons via a succession of absorbers and scintillators. This makes it crucial for physics analyses with hadronic jets or missing transverse energy. The HCAL extends between $1.77 < r < 2.95$ m where r is the radius in the transverse plane with respect to the beam. Due to space limitations, the HCAL needs to be as small as possible and is made from materials with short interaction lengths - the length needed for absorbing 36.7% of the hadrons. The quality of the energy measurements is dependant on the fraction of the hadronic shower that can be detected. Therefore, the HCAL barrel (HB) inside the solenoid is reinforced by an outer hadronic calorimeter between the solenoid and muon detectors (HO, see Figure 2.10), using the solenoid as extra absorber. This increases the thickness to 12 interaction lengths. Furthermore, it should be as hermetic as possible and extend to large pseudo rapidity values. The HB and HO provide measurements for $|\eta| < 1.3$, while an end cap on each side (HE,$1.3 < |\eta| < 3$) and a forward calorimeter (HF, $|\eta| < 5.2$) extend the pseudo rapidity range.

The HB is made of 16 absorber plates where most of them are built from brass and others are made from stainless steal and is about five to ten intercation lengths thick. The HE is also composed of brass absorber plates and has a thickness corresponding to approximately ten interaction lengths. The HF experiences intense particle fluxes with an energy of 760 GeV deposited on average in a proton interaction at a center of mass of 14 TeV, compared to 100 GeV in the rest of the detector. Therefore, these are Cherenkov light detectors made of radiation hard quartz fibers. The main causes of such large energy events are high energy muons, cosmic particles and charged particles from late showering hadrons. During Run I, it became clear that the glass windows of the PMTs had to be replaced which was done during LS1 [68]

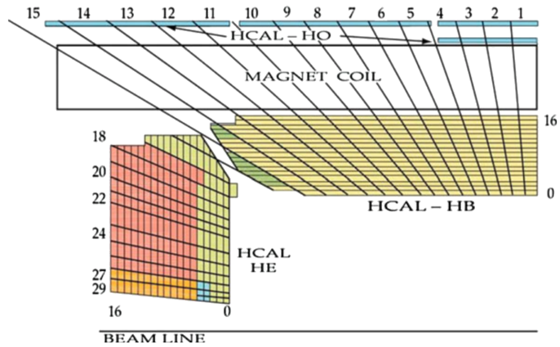

Figure 2.10: Tower segmentation for one quarter of the HCAL displayed in the rz plane[46].

2.2.2.4 Electromagnetic calorimeter

The electromagnetic calorimeter (ECAL) is designed to measure the energy of photons and electrons and covers $|\eta| < 3$. It is an hermetic, homogeneous detector and consists of 75 848 lead tungstate ($PbWO_4$) crystals. These crystals have a fast response time - 80% of the light is emitted within 25 ns - and are radiation hard. The electromagnetic showers produced by passing electrons or photons ionize the crystal atoms which emit a blue-green scintillation light, that is collected by silicon avalanche photodiodes (APDs) in the barrel and vacuum phototriodes (VPTs) in the end caps. The crystals and the APD response is sensitive to temperature changes and require a stable temperature.

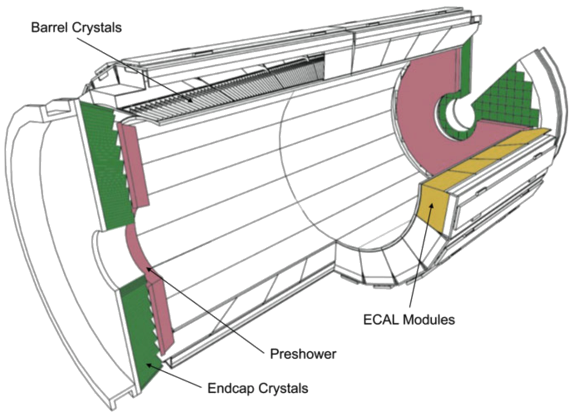

Figure 2.11: Schematic cross section of the electromagnetic calorimeter[46].

There are three regions: a central barrel (EB), a endcap region (EE) and a preshower (ES) (Figure 2.11). The EB has an inner radius of 129 cm and corresponds to a pseudo rapidity of $0 < |\eta| < 1.479$. At a distance of 314 cm from the vertex and covering a pseudo rapidity of $1.479 < |\eta| < 3.0$, are the EE. They consist of semi-circular aluminium plates from which structural units of 5×5 crystals (super crystals) are supported. The ES is placed in front of the crystal calorimeter over the end cap pseudo rapidity range with two planes of silicon strip detectors as active elements.

The electromagnetic shower will typically involve more than one channel. More than 90% of the energy of a 35 GeV electron or photon is contained in a 5 × 5 matrix of crystals. Therefore, a clustering algorithm is performed in order to associate the energy deposits to the particles impinging the calorimeter. The achieved precision[69] for the barrel is 2.10^{-3} rad in ϕ and 10^{-3} in η . For the end caps this is 5.10^{-3} rad in ϕ and 2.10^{-3} in η . The energy is reconstructed by a super cluster algorithm, taking into account energy radiated via bremsstrahlung or conversion:

$$E_{e/\gamma} = GF_{e/\gamma} \sum_{i \in cluster} S_i(t) V C_i A_i, \tag{2.5}$$

where G is the absolute energy scale in GeV/ADC, F the energy containment corrections (depends on type of particle, its energy and pseudo rapidity, eg shower leakage and bremsstrahlung losses for electrons), $S(t)$ the relative channel variation with time, C the relative channel response and A the amplitude in ADC counts. The energy resolution is given by

$$\frac{\sigma(E)}{E} = \frac{2.8\%}{\sqrt{E}} \oplus \frac{0.128}{E(GeV)} \oplus 0.3\%, \tag{2.6}$$

in the absence of a magnetic field, where the contributions come from the stochastic, noise and constant terms respectively. The dominating term is the constant term ($E_{shower} \approx 100GeV$) and thus the performance is highly dependent on the quality of calibration and monitoring .

In Run I, the energy reconstruction happened via a weighted sum of the digitized samples[70]. For Run II however, the reconstruction had to be made more resistant for out of time pile up and a multi-fit approach has been set in to place. In this approach, the pulse shape is modelled as a sum of one in-time pulse plus the out of time pulses [69]. The energy resolution is less than 2% in the central barrel region and 2-5 % elsewhere.

2.2.2.5 Inner tracking system and operations

The tracking system (tracker) [71] is the detecting unit closest to the point of interaction. Responsible for the reconstruction of trajectories from charged particles with $|\eta| < 2.5$ that are bent by the magnetic field, it provides a measurement of the momentum. The tracker is also responsible for the determination of the interaction point or vertex. It should be able to provide high granularity as well as speed, and be able to endure high radiation. For this reason, the CMS collaboration choose silicon detector technology.

The tracking system consists of a cylinder of 5.8 m long and 2.5 m in diameter. It is immersed in a co-axial magnetic field of 3.8 T due to the solenoid. As shown Figure 2.12, the tracker is built up from a large silicon strip tracker with a small silicon pixel inside. The inner region, pixel ($4.4 < r < 10.2$ cm), gets the highest flux of particles. Therefore, pixel silicon sensors of 100 × 150 µm aree used. It consists of three cylindrical barrels that are complemented by two discs of pixel modules at each side. The silicon strip tracker ($20 < r < 116$ cm) has three subdivisions. The Tracker Inner Barrel and Discs (TIB, TID, see Figure 2.14) are composed of four barrel layers accompanied by three discs at each end. The outer part of the tracker - Tracker Outer Barrel (TOB) - consists of 6 barrel layers. In the outer discs, there are nine discs of silicon sensors, referred to as Tracker End Caps (TEC).

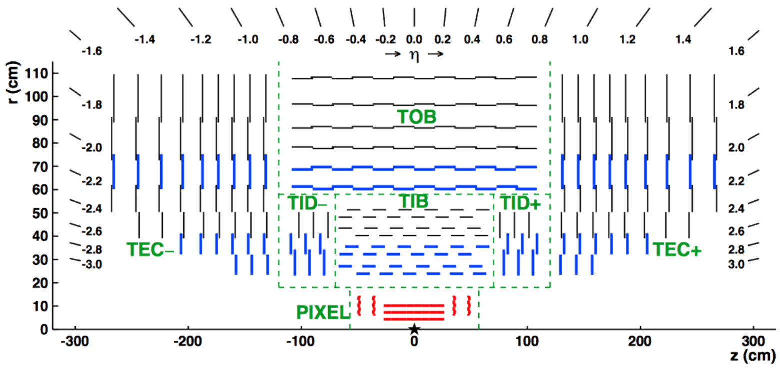

Figure 2.12: Schematic cross section of the top half of the CMS tracking system in the rz plane. The centre of tracker is shown with a star and corresponds to the approximate position of the proton collision point. The green dashed lines are an indication for each named tracker subsystem. The strip tracker modules that provide two-dimensional hits are shown by thin, black lines, while those able to reconstruct three-dimensional hit positions are shown by thick, blue lines. The pixel modules, shown in red, also provide three-dimensional hits. [57]

The pixel, shown in Figure 2.13 has 1440 modules that cover an area of about 1 m^2 and have 66 million pixels. It provides a three-dimensional position measurement of the hits arising from the interaction from charged particles with the sensors. In transverse coordinate ($r\phi$), the hit position resolution is about 10 µm, while 20-40 µm is obtained in the longitudinal coordinate (z). The sensor plane position provides the third coordinate. The silicon strip trackers consists of 15 148 single sided modules placed in the TIB, TID and the first four rings of the TEC. They provide 9.3 million readout channels. In the TOB and the outer three rings of the TEC, double sided modules are used. These modules are constructed from two back-to-back single sided modules, where one module is rotated through a stereo angle. This covers an active area of about 198 m^2. The TIB and TID provide position measurements in $r\phi$ with a resolution of approximately 13-38 µm, while the TOB provides a resolution of about 18-47 µm. The resolution in the z direction is approximately 230 µm in the TIB/TID and 530 µm in the TOB. To allow overlay and avoid gaps in acceptance, each module is shifted slightly in r or z with respect to its neighbouring modules within a layer. With this detector lay out, at least nine points per charged particle trajectory can be measured in an $|\eta|$ range up to 2.4.

During the first data taking period of the LHC (2010 to 2013), the tracker operated at +4°C. With the higher LHC beam intensities from 2015 onwards, the tracker needs to be operated at much lower temperatures. This is due to the fact with intense irradiation, the doping concentration changes, the leakage current increases proportional to the fluence and the charge collection efficiency decreases due to charge trapping. Mostly the leakage current (I) is affected by the temperature change:

$$I \propto T^2 e^{-\frac{E_g}{2kT}}, \tag{2.7}$$

where T is the operating temperature, E_g the band gap and k the Boltzmann constant. There is approximately a factor 15 between the leakage currents at room temperatures and at -10 °C.

Figure 2.13: The pixel barrel being re-installed after the Long Shutdown in 2015, around the beam pipe at CMS[72]

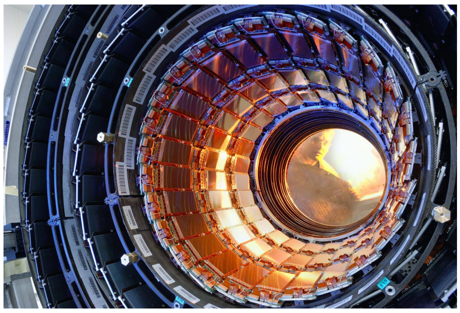

Figure 2.14: First half of the inner tracker barrel, consisting of three layers of silicon modules.[73]

During the LS1, the CMS cooling plant was refurbished[74](Figure 2.16) and the fluorocarbon cooling system overhauled. To help to suppress the humidity inside the tracker, new methods for vapour sealing and insulation were applied (Figure 2.15. Furthermore, several hundred high-precision sensors are used to monitor the humidity and temperature. In order to get as dry air as possible, a new dry-gas plant provides eight times more dry gas (air or nitrogen) than during the first run, and allows regulation if the flow. As final addition, the cooling bundles outside the tracker are equipped with heater wires and temperature sensors in order to maintain safe operations above the cavern dew point For the data taking in 2015-2016, the tracker operated at $-15°$C.

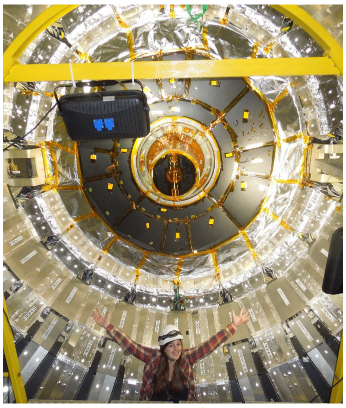

Figure 2.15: Tracker bulkhead being put into closed state with insulation pieces installed during an early trial in fall 2013

Figure 2.16: New Tracker high-capacity dry-gas plant with membrane separation system[61]

Track reconstruction

An iterative tracking algorithm is responsible for the reconstruction of the tracks made by charged particles in the inner tracking system. Each iteration consists of four steps[58]: the track-seed generation, the pattern recognition algorithm, removal of track-hit ambiguities and a final track fit.

The seed generation is the first step. It consists of finding reconstructed hits that are usable for seeding the subsequent track-finding algorithm. They are identified from a group of at least three reconstructed hits in the tracker, or from a pair of hits while requiring the origin of the track segment to be compatible with the nominal beam-collision point. Since the pixel has a higher granularity compared to the strip tracker, its seed generation efficiency is higher. The overall efficiency exceeds 99%. The second step of each iteration, the pattern recognition algorithm, uses the seeds as a starting point for a Kalman filter method [66, 67]. This algorithm extrapolates the seed trajectory towards the next tracker layer taking into account the magnetic field and multiple scattering effects. The track parameters are updated when a compatible hit in the next layer is found. This procedure continues until the outermost layer us reached. Since the Kalman filter method can result in multiple tracks associated to the same seed, or different tracks sharing the same hits, a removal of ambiguities is necessary. This ambiguity resolving is done by removing tracks that are sharing too many hits from the list of track candidates. The tracks with highest number of hits or with the lowest χ^2 if the track fit is kept. The updated track parameters are then refitted using the Kalman filter method, where all hits found in the pattern recognition step are taken into account. The fit is done twice - once outwards from the beam line towards the calorimeters, and inwards from the outermost track hit to the beam line -, improving the estimation of the track parameters.

All hits that are unambiguously associated to the final track are removed from the list of available hits. In order to associate the remaining hits, the procedure is repeated with looser track reconstruction criteria. The use of the iterative track reconstruction procedure has a high track finding efficiency, where the fake track reconstruction rate is negligible. For muons, this results in a global track reconstruction efficiency exceeding 98%, and 75-98% for charged hadrons.

Primary vertex reconstruction

The primary vertex reconstruction should be able to meausre the location of all proton interaction vertices in each event: the signal vertex an all vertices from pile up events. It consists of a vertex finding and a vertex fitting algorithm and happens in three steps. Tracks are selected to be consistent with being produced promptly in the primary interaction by imposing requirements on the track parameters[71] By grouping reconstructed tracks according to the z coordinate of their closest approach to the beam line, vertices for all interaction in the same beam crossing are found, at CMS this is done by a deterministic annealing algorithm [75] . On top of this, a vertex fitting algorithm like the Adaptive Vertex fitter [76], is performed. This creates the three-dimensional primary-vertex position. With this fit, the contribution from long-lived hadron decays is reduced by down weighting the tracks with a larger distance to the vertex. The primary vertex corresponding to the highest sum of squared track transverse momenta is noted as the point of the main interaction. The resolution on the primary vertex is about 14 μm in $r\phi$ and about 19 μm in the z direction for primary vertices with the sum of the track $p_T > 100$ GeV for 2016 data taking.

2.2.3 Data acquisition

At a design luminosity of 10^{34} $1/(\mathrm{m}^2\,\mathrm{s})$, the proton interaction rate exceeds 1 GHz. This makes it impossible for the CMS experiment to store all the data generated. For this, a two level trigger system has been put in place. The first level (Level-1) is a custom hardware system, while a second level (HLT) is software based running on a large farm of computers. In run II, with the increase in centre of mass energy and a higher luminosity, a larger number of simultaneous inelastic collisions per crossing is expected with respect to run I. For this, the CMS Level-1 has been upgraded [77].

CMS Level-1 trigger

The Level-1 trigger has to be a flexible, maintainable system, capable of adapting to the evolving physics programme of CMS [78]. Its output rate is restricted to 100 kHz imposed by the CMS readout electronics. It is implemented by custom hardware and selects events containing candidate objects - eg ionization deposits consistent with a muon, or energy clusters corresponding to an electron / photon / tau lepton / missing transverse energy / jet. Collisions with large momenta can be selected by using scalar sum of the transverse momenta of the jets.

By buffering the raw data from the CMS subdetectors in front-end drivers, the level-1 trigger has a pipeline memory of 3.2 µs to decide whether to keep an event or reject it. The trigger primitives (TP) from the calorimeters and muon detectors are processed in several steps and combined into a global trigger. This information is then combined with the input from the other subsystems for the HLT. The separate inputs are synchronized to each other and the LHC orbit clock and sent to the global trigger module. Here, level-1 trigger algorithms are performed within 1 µs to decide whether to keep the event.

For run II, all hardware, software, databases and the timing control system have been replaced. The main changes are that the muon system now uses the redundancy of three muon detector system earlier to make a high resolution muon trigger. Other upgrades are that the calorimeter system isn't bound any more for streaming data the data and the global trigger has more level-1 trigger algorithms.

CMS HLT trigger

The HLT is an array of commercially available computers with programmable menu that has output rate of on average 400 Hz for off-line event storage. The data processing is based on a HLT path. This is a set of algorithmic steps to reconstruct objects and make selections on them. Here, the information of all sub detectors can be used to perform algorithms on higher level reconstructed objects.

2.2.4 CMS computing model

The selected data is stored, processed and dispersed via the Worldwide Large Hadron Collider GRID (WLCG)[79, 80]. This has a tiered structure that function as a single, coherent system:.

At CERN, a single Tier-0 is located. The raw data collected by CMS is archived here, and a first reconstruction of the data is done. This data is then already in a file format usable for physics analysis. Furthermore, it is able to reprocess data when new calibrations are made available. The Tier-0 site distributes this data to a total of seven Tier-1 centres. They carry out data reprocessing and store real data as well as simulated data. The Tier-1 further distribute the data to over 50 Tier-2 centres. These make the data accessible for physics analysis and are also being used for the production of simulated data. The data is made accessible for physicists around the world.

3 Analysis techniques

3.1 Event generation

In order to compare reconstructed data with theoretical predictions, collision events are generated and passed through a simulation of the CMS detector and an emulation it readout. For the detector simulation, a so-called Full Simulation package [81, 82] based on the Geant4 toolkit [83] is employed. It allows a detailed simulation of the interactions of the particles with the detecor material.

3.1.1 Fundamentals of simulating a proton collision

The procedure of to generate $\mathrm{pp} \rightarrow \mathrm{X}$ events can be subdivided into sequential steps [84–86], as shown in Figure 3.1.

Each proton consists of three valence quarks $(\mathrm{u\ u\ d})$ and many sea quarks and gluons, called partons. These partons emerge from each proton within a certain probability density $f(x, Q^2)$, determined by the momentum fraction x carried by the parton and the momentum transfer Q^2. The parton density functions (PDF) [87–89] give the momentum distribution of the proton amongst its partons.

The interaction of two incoming protons is often soft and elastic leading to events that are not interesting in the framework of this thesis. More interesting are the hard interaction between two partons from the incoming protons. The matrix elements (ME) of a hard scattering process of interest is the starting point of the generation of events. Monte Carlo techniques are used to sample the corresponding cross section integral and the resulting sample of events reflect the probability distribution of a process over its final state phase space. After obtaining the sample of events of the hard interaction, a parton shower (PS) program is used to simulate the hadronisation of final state partons into hadrons which then can also decay further. Additionally, radiation of soft gluons or quarks from initial or final state partons is simulated. These are respectively reffered to as initial state radiation (ISR) or final state radiation (FSR). Contributions from soft secondary interactions, the so-called underlying event (UE), and colour reconnection effects are also taken into account. A brief overview of the employed programs used for the event generation of the signal and main background processes used in the search presented in the thesis are given in Section 3.1.2.

NOTE: Should I add more details?

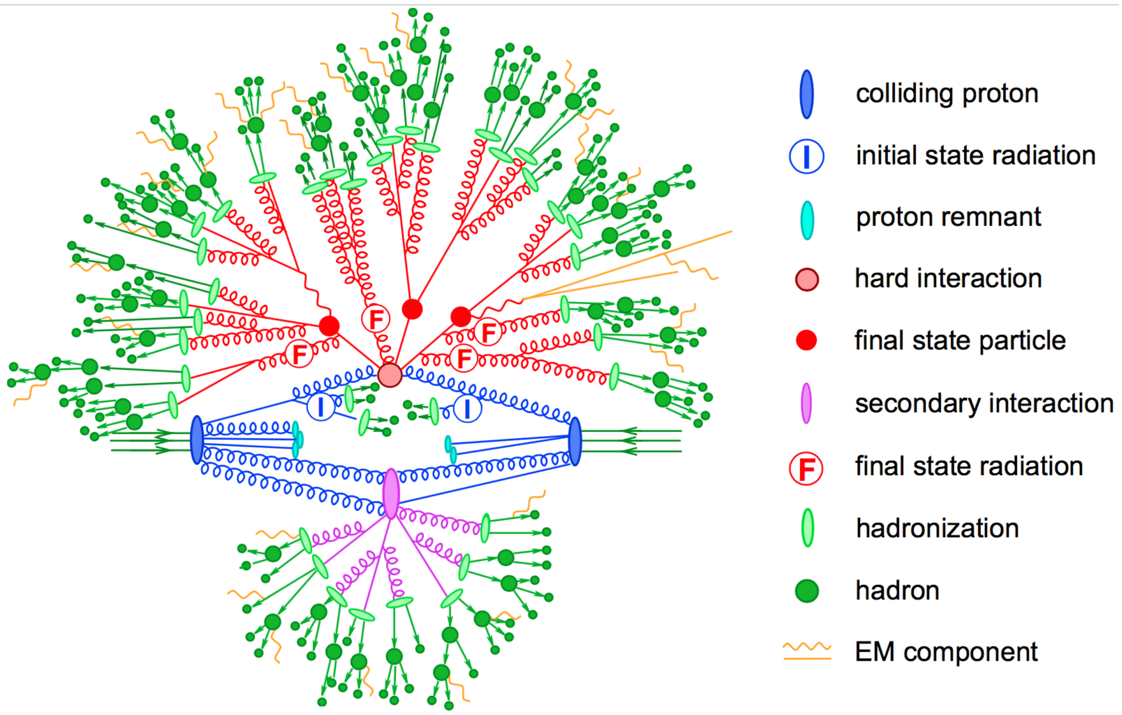

Figure 3.1: Sketch of a hadron collision as simulated by a Monte-Carlo event generator. The red blob in the center represents the hard collision, surrounded by a tree-like structure representing Bremsstrahlung as simulated by parton showers. The purple blob indicates a secondary hard scattering event. Parton-to-hadron transitions are represented by light green blobs, dark green blobs indicate hadron decays, while yellow lines signal soft photon radiation. Figure taken from [86].

3.1.2 Programs for event generation

The FEYNRULES package [90] allows the calculation of the Feynman rules in momentum space for any quantum field theory model. By use of a Lagrangian, the set of Feynman rules associated with this Lagrangian are calculated. Via the `Universal Feynrules Output` (UFO) [91] the results are then passed to matrix element generators.

The `MadGraph` program [92] is used to interpret the physics model and calculate the corresponding Feynman diagrams and matrix elements. After this, `MadEvent` [**bibid**] is used to calculate the corresponding partons. These generated parton configurations are then merged with `Pythia` [93–95] parton showers using the MLM merging scheme [96].

The `MadGraph5_aMC@NLO` program [97] combines the leading order[1] (LO) `MadGraph` [92] and the `aMC@NLO` program into a common framework. This combination supports the generation of samples at LO or next to leading order (NLO) together with a dedicated matching to parton showers using the MLM [96] or FXFX [98] schemes respectively. The FXFX scheme produces a

[1] A leading order process is a process which involves the minimal amount of particles. This also indicated as a tree-level Feynman diagram. Every added interaction vertex increases the order. To obtain the highest precision of an observable quantity the process should consider an infinite amount of orders. Computational limitations limits the process usually the next to leading order.

certain fraction of events with negative weights originating from the subtraction of amplitudes that contain additional emissions from the NLO matrix element to prevent double-counting.

The POWHEG box (versions 1,2) [99–104] contains predefined implementations of various processes at NLO. It applies the POWHEG method for ME- to PS- matching, where the hardest radiation generated from the ME has priority over subsequent PS emission to remove the overlap with the PS simulation.

The JHU generator (version 7.02) [105–108] is used to generate the parton level information including full spin and polarization correlations. It is commonly used for studying the spin an parity properties of new resonances such as $\mathrm{ab} \rightarrow \mathrm{X} \rightarrow \mathrm{VV}$, where $\mathrm{V} = \mathrm{Z}, \mathrm{W}, \gamma$).

The generation of events from processes involving the production and decay of resonances creates a computational heavy load, especially at NLO. The narrow width approximation the resonant particle is assumed to be on-shell. This makes the production and decay amplitude factorize, allowing to perform the simulation of the production and decay of heavy resonances like top quarks or Higgs bosons to be performed in separate steps. The MadSpin program [109] extends this approach and accounts for off-shell effects through a partial reweighting of the events. Additionally, spin correlation effects between production and decay products are taken into account.

The Pythia program (versions 6,8) [93–95] generates events of various processes at LO. Usually in the analysis, it is however only used for its PS simulation and it is interfaced with other LO and NLO event generators to perform subsequent parton showering, hadronisation, and simulation of the underlying event. In this thesis the underlying event tunes [110] are the CUETP8M2T4, CUETP8M1 and CUETP8M2.

The detector response is simulated via the Geant4 [83] program. This program tracks the particles through the detector material via a detailed description of the detector and generates several hits throughout several sensitive layers. In addition, the response of the detector electronics to these hits are simulated.

3.1.3 Generating FCNC top-Z interactions

The FCNC processes are generated by interfacing the Lagrangian in Equation 1.23 with MadGraph5_aMC@NLO by means of the FeynRules package and the Universal Feynrules Output format. The complex chiral parameters are arbitrary chosen to be $f^{\mathrm{L}}_{\mathrm{Xq}} = 0$ and $f^{\mathrm{R}}_{\mathrm{Xq}} = 1$. The signal rates are estimated by use of the MadGraph5_aMC@NLO program for estimating the partial widths. The anomalous couplings are left free to float for this estimation, and only one coupling allowed to be non-vanishing at a time. The results are presented in Table 3.1. The anomalous single top cross sections are calculated by convolution of the hard scattering matrix elements with the LO order set of CTEQ6 partons densities [111]. The NLO effects are modelled by multiplying each LO cross section by a global k-factor. The LO single top production cross section and the global k-factors for the top-Z production are shown in Table 3.2. The hard scattering events are then matched to parton showers to Pythia to account for the simulation of the QCD environment relevant for hadronic collisions.

Table 3.1: Leading order partial widths related to the anomalous decay modes of the top quark, where the new physics scale Λ is given in GeV.

Anomalous coupling	vertex	Partial decay width (GeV)	
κ_{gqt}/Λ	t g u	3.665220 10^5	$\left(\kappa_{tgu}/\Lambda\right)^2$
	t g c	3.664620 10^5	$\left(\kappa_{tgc}/\Lambda\right)^2$
$\kappa_{t\gamma q}/\Lambda$	t γ u	1.989066 10^4	$\left(\kappa_{t\gamma u}/\Lambda\right)^2$
	t γ c	1.988904 10^4	$\left(\kappa_{t\gamma c}/\Lambda\right)^2$
κ_{tZq}/Λ	t Z u	1.637005 10^4	$\left(\kappa_{tZu}/\Lambda\right)^2$
	t Z c	1.636554 10^4	$\left(\kappa_{tZc}/\Lambda\right)^2$
ζ_{tZq}	t Z u	1.685134 10^{-1}	$\left(\zeta_{tZu}\right)^2$
	t Z c	1.684904 10^{-1}	$\left(\zeta_{tZc}\right)^2$
η_{tHq}	t H u	1.904399 10^{-1}	$\left(\eta_{tHu}\right)^2$
	t H c	1.904065 10^{-1}	$\left(\eta_{tHc}\right)^2$

Table 3.2: Leading order single top production cross section for $pp \to tZ$ or $\bar{t}\,Z$, where the new physics scale is given in GeV. The NLO k—factors are given in the last column.

Anomalous coupling	Cross section (pb)		NLO k—factor
κ_{tgu}/Λ	3.272 10^7	$\left(\kappa_{tgu}/\Lambda\right)^2$	1.00
κ_{tgc}/Λ	3.021 10^6	$\left(\kappa_{tgc}/\Lambda\right)^2$	1.00
$\kappa_{t\gamma u}/\Lambda$	2.260 10^5	$\left(\kappa_{t\gamma u}/\Lambda\right)^2$	1.00
$\kappa_{t\gamma c}/\Lambda$	2.654 10^4	$\left(\kappa_{t\gamma c}/\Lambda\right)^2$	1.00
κ_{tZu}/Λ	1.728 10^6	$\left(\kappa_{tZu}/\Lambda\right)^2$	1.40
κ_{tZc}/Λ	2.040 10^5	$\left(\kappa_{tZc}/\Lambda\right)^2$	1.40
ζ_{tZu}	7.484	$\left(\zeta_{tZu}\right)^2$	1.40
ζ_{tZc}	1.038	$\left(\zeta_{tZc}\right)^2$	1.40

The top pair cross sections are derived from the SM $t\bar{t}$ cross section, calculated with `MadGraph5_aMC@NLO` at NLO ($\sigma_{t\bar{t}} = 6.741\ 10^2$pb), and considering the decay $t\bar{t} \to (bW^{\pm})(Xqt)$. The branching ratio $\mathcal{B}(t \to bW^{\pm})$ is assumed to be equal to one and the FCNC branching ratio is calculated as

$$\mathcal{B}(t \to qX) = \frac{\Gamma_{t\to qX}}{\Gamma_t^{SM} + \Gamma_t^{FCNC}} \approx \frac{\Gamma_{t\to qX}}{\Gamma_t^{SM}}, \tag{3.1}$$

where $\Gamma_{t\to qX}$ is given in Table 3.1, and the assumption $\Gamma_t^{FCNC} \ll \Gamma_t^{SM}$ is made . In Table 3.3 the resulting NLO cross sections for the top-Z FCNC interactions are given.

NOTE: these partial widths are at LO, how does this relate to NLO that is used? Or is there no difference?

Table 3.3: Next to leading order top pair cross section for the top-Z FCNC interactions with with a full leptonic decay.

Anomalous coupling	Process	Cross section (pb)	
κ_{tZu}/Λ	$t\bar{t} \to (b\ell^+\nu)(\bar{u}\ell^+\ell^-)$	$2.727008\ 10^5$	$\left(\kappa_{tZu}/\Lambda\right)^2$
	$t\bar{t} \to (\bar{b}\ell^-\bar{\nu})(u\ell^+\ell^-)$	$2.727008\ 10^5$	$\left(\kappa_{tZu}/\Lambda\right)^2$
κ_{tZc}/Λ	$t\bar{t} \to (b\ell^+\nu)(\bar{c}\ell^+\ell^-)$	2.72625710^5	$\left(\kappa_{tZc}/\Lambda\right)^2$
	$t\bar{t} \to (\bar{b}\ell^-\bar{\nu})(c\ell^+\ell^-)$	$2.726257\ 10^5$	$\left(\kappa_{tZc}/\Lambda\right)^2$
ζ_{tZu}	$t\bar{t} \to (b\ell^+\nu)(\bar{u}\ell^+\ell^-)$	2.827184	$\left(\zeta_{tZu}\right)^2$
	$t\bar{t} \to (\bar{b}\ell^-\bar{\nu})(u\ell^+\ell^-)$	2.827184	$\left(\zeta_{tZu}\right)^2$
ζ_{tZc}	$t\bar{t} \to (b\ell^+\nu)(\bar{c}\ell^+\ell^-)$	2.806801	$\left(\zeta_{tZc}\right)^2$
	$t\bar{t} \to (\bar{b}\ell^-\bar{\nu})(c\ell^+\ell^-)$	2.806801	$\left(\zeta_{tZc}\right)^2$

3.1.4 Generating SM background events

The SM tZqevents were generated using the `MadGraph5_aMC@NLO` generator, interfaced with `Pythia` version 8.2 [95] for parton showering and hadronisation. The WZ+jets, $t\bar{t}$Z and $t\bar{t}$W samples are produced using the `MadGraph5_aMC@NLO`(version 5.222) [97], which includes up to one hadronic jet at next to leading order (NLO) QCD accuracy. Other minor background (e.g. WW, ZZ, tWZ and $t\bar{t}$H) are simulated using different generators such as `POWHEG` [112–115] and `MadGraph` [92] at leading order QCD accuracy. All events are interfaced to `Pythia` for parton shower and hadronisation.

The complete list of SM samples is given in Table 3.4 , along with their cross sections. The cross sections without a reference are coming from the generator with which the sample has been made, for some of them the uncertainties are provided by the Generator Group. For each MC sample, the integrated luminosity that the sample represents is estimated as the number of simulated events divided by the cross section of the generated process. For processes generated with `MadGraph5_aMC@NLO`, the effective number of simulated events is used, taking into account positive and negative event weights. The correction factor for those events is defined as

NOTE: Add source

$$C = \frac{\text{Nb. of pos. weights} + \text{Nb. of neg. weights}}{\text{Nb. of pos. weights} - \text{Nb. of neg. weights}} \times \text{mc baseweight} \tag{3.2}$$

Table 3.4: SM MC samples used in this analysis with their corresponding cross section and MadGraph5_aMC@NLO correction C when applicable. The generators used for each sample are indicated.

Process	Generator	Cross section (pb)	C
$WZ \rightarrow 3\ell\nu$	MadGraph5_aMC@NLO+Pythia	5.26	1.61
tZq with $Z \rightarrow \ell^+\ell^-$	MadGraph5_aMC@NLO+Pythia	0.0758	3.77
tqH with $H \rightarrow ZZ \rightarrow \ell^+\ell^-\ell^+\ell^-$	JHU+Pythia	$8.80\ 10^{-6}$	-
$t\bar{t}W$+jets with $W \rightarrow \ell\nu$	MadGraph5_aMC@NLO+MadSpin+Pythia	0.2043 ± 0.0020	1.94
$t\bar{t}Z$ containing at least $2\ell\ +2\nu$, with $m_{\ell\ell} > 10$ GeV	MadGraph5_aMC@NLO+Pythia	0.2529 ± 0.0004	2.15
$t\bar{t}H$,no $b\bar{b}$ decays	POWHEG+Pythia	0.2151	-
$t\bar{t}H$, $b\bar{b}$ decays	POWHEG+Pythia	0.2934	-
$WW \rightarrow 2\ell2\nu$	POWHEG+Pythia	12.178	-
$ZZ \rightarrow 4\ell$	POWHEG+Pythia	0.3366	-
WZZ	MadGraph5_aMC@NLO+Pythia	0.05565	1.14
ZZZ	MadGraph5_aMC@NLO+Pythia	0.01398	1.17
single toptWZ, with $Z_\mu \rightarrow \ell^+\ell^-$	MadGraph+Pythia	0.001123	-
single top t-channel $\bar{t}$	POWHEG+MadSpin+Pythia	$44.33\ ^{+1.76}_{-1.49}$	-
single top t-channel t	POWHEG+MadSpin+Pythia	$26.38\ ^{+1.32}_{-1.18}$	-
single top $\bar{t}W$	POWHEG+Pythia	35.85 ± 0.90 (scale) ± 1.70 (pdf)	-
single top tW	POWHEG+Pythia	35.85 ± 0.90 (scale) ± 1.70 (pdf)	-
$t\bar{t}$	POWHEG+Pythia	$831.76\ ^{+19.77+35.06}_{-29.20-35.06}$	-
Z/γ^* +jets, with $m_{\ell\ell} >$ 50GeV	MadGraph5_aMC@NLO+Pythia	$3 \times(1921.8 \pm 0.6 \pm 33.2)$	1.49
Z/γ^* +jets, with 10 GeV $< m_{\ell\ell} <$ 50 GeV	MadGraph+Pythia	18610	-

3.2 Multivariate analysis techniques: Boosted Decision Trees

3.3 Template-based fitting

4 Event reconstruction

After the detector simulation described in Section **??**, the simulated data has the exact same format as the real collision data recorded at the CMS experiment. Therefore the same software can be used for the reconstruction of both simulation and real data. In this Chapter, the event reconstruction for physics analysis is shown.

5 The search for FCNC involving a top quark and a Z boson

Bibliography

[1] Michael E Peskin and Daniel V Schroeder: **An introduction to quantum field theory; 1995 ed.** Includes exercises. Boulder, CO: Westview, 1995. URL: https://cds.cern.ch/record/257493 (see pp. 1, 5).

[2] Nadia Robotti: **The discovery of the electron: I**. In: *European Journal of Physics*, **18**:3 (1997), p. 133. URL: http://stacks.iop.org/0143-0807/18/i=3/a=002 (see p. 1).

[3] C. Patrignani et al.: **Review of Particle Physics**. In: *Chin. Phys.*, **C40**:10 (2016), p. 100001. DOI: 10.1088/1674-1137/40/10/100001 (see pp. 2–3, 6).

[4] S. Abachi et al.: **Observation of the top quark**. In: *Phys. Rev. Lett.*, **74**: (1995), pp. 2632–2637. DOI: 10.1103/PhysRevLett.74.2632. arXiv: hep-ex/9503003 [hep-ex] (see p. 2).

[5] F. Abe et al.: **Observation of top quark production in $\bar{p}p$ collisions**. In: *Phys. Rev. Lett.*, **74**: (1995), pp. 2626–2631. DOI: 10.1103/PhysRevLett.74.2626. arXiv: hep-ex/9503002 [hep-ex] (see p. 2).

[6] Serguei Chatrchyan et al.: **Observation of a new boson at a mass of 125 GeV with the CMS experiment at the LHC**. In: *Phys. Lett.*, **B716**: (2012), pp. 30–61. DOI: 10.1016/j.physletb.2012.08.021. arXiv: 1207.7235 [hep-ex] (see pp. 2, 13).

[7] Georges Aad et al.: **Observation of a new particle in the search for the Standard Model Higgs boson with the ATLAS detector at the LHC**. In: *Phys. Lett.*, **B716**: (2012), pp. 1–29. DOI: 10.1016/j.physletb.2012.08.020. arXiv: 1207.7214 [hep-ex] (see pp. 2, 13).

[8] Nicola Cabibbo: **Unitary Symmetry and Leptonic Decays**. In: *Phys. Rev. Lett.*, **10**: (12 June 1963), pp. 531–533. DOI: 10.1103/PhysRevLett.10.531 (see p. 5).

[9] S. L. Glashow, J. Iliopoulos, and L. Maiani: **Weak Interactions with Lepton-Hadron Symmetry**. In: *Phys. Rev. D*, **2**: (7 Oct. 1970), pp. 1285–1292. DOI: 10.1103/PhysRevD.2.1285 (see p. 5).

[10] B.J. Bjørken and S.L. Glashow: **Elementary particles and SU(4)**. In: *Physics Letters*, **11**:3 (1964), pp. 255–257. DOI: https://doi.org/10.1016/0031-9163(64)90433-0 (see p. 5).

[11] Luciano Maiani: **The GIM Mechanism: origin, predictions and recent uses**. In: *Proceedings, 48th Rencontres de Moriond on Electroweak Interactions and Unified Theories: La Thuile, Italy, March 2-9, 2013*. 2013, pp. 3–16. arXiv: 1303.6154 [hep-ph]. URL: https://inspirehep.net/record/1225307/files/arXiv:1303.6154.pdf (see p. 5).

[12] Patrick Koppenburg and Sebastien Descotes-Genon: **The CKM Parameters**. In: (2017). arXiv: 1702.08834 [hep-ex] (see p. 6).

[13] J. A. Aguilar-Saavedra: **Top flavor-changing neutral interactions: Theoretical expectations and experimental detection**. In: *Acta Phys. Polon.*, **B35**: (2004), pp. 2695–2710. arXiv: hep-ph/0409342 [hep-ph] (see pp. 6, 8–9).

[14] Yorikiyo Nagashima: **Beyond the standard model of elementary particle physics**. Weinheim, Germany: Wiley-VCH Verlag, 2014. URL: http://www-spires.fnal.gov/spires/find/books/www?cl=QC793.2.N34::2014 (see p. 6).

[15] Y. Fukuda et al.: **Evidence for oscillation of atmospheric neutrinos**. In: *Phys. Rev. Lett.*, **81**: (1998), pp. 1562–1567. DOI: 10.1103/PhysRevLett.81.1562. arXiv: hep-ex/9807003 [hep-ex] (see p. 7).

[16] Y. Abe et al.: **Indication of Reactor $\overline{\nu}_e$ Disappearance in the Double Chooz Experiment**. In: *Phys. Rev. Lett.*, **108**: (13 Mar. 2012), p. 131801. DOI: 10.1103/PhysRevLett.108.131801 (see p. 7).

[17] P. A. R. Ade et al.: **Planck 2015 results. XIII. Cosmological parameters**. In: *Astron. Astrophys.*, **594**: (2016), A13. DOI: 10.1051/0004-6361/201525830. arXiv: 1502.01589 [astro-ph.CO] (see p. 7).

[18] P. J. E. Peebles and Bharat Ratra: **The Cosmological constant and dark energy**. In: *Rev. Mod. Phys.*, **75**: (2003), pp. 559–606. DOI: 10.1103/RevModPhys.75.559. arXiv: astro-ph/0207347 [astro-ph] (see p. 7).

[19] A. D. Sakharov: **Violation of CP Invariance, c Asymmetry, and Baryon Asymmetry of the Universe**. In: *Pisma Zh. Eksp. Teor. Fiz.*, **5**: (1967). [Usp. Fiz. Nauk161,61(1991)], pp. 32–35. DOI: 10.1070/PU1991v034n05ABEH002497 (see p. 7).

[20] Gustavo Burdman: **New solutions to the hierarchy problem**. In: *Braz. J. Phys.*, **37**: (2007), pp. 506–513. DOI: 10.1590/S0103-97332007000400006. arXiv: hep-ph/0703194 [hep-ph] (see p. 7).

[21] T. et al. Aaltonen: **Search for the Flavor-Changing Neutral-Current Decay $t \to Zq$ in $p\overline{p}$ Collisions at $\sqrt{s} = 1.96$ TeV**. In: *Phys. Rev. Lett.*, **101**: (19 Nov. 2008), p. 192002. DOI: 10.1103/PhysRevLett.101.192002 (see p. 8).

[22] Victor Mukhamedovich Abazov et al.: **Search for flavour changing neutral currents via quark-gluon couplings in single top quark production using 2.3 fb^{-1} of $p\bar{p}$ collisions**. In: *Phys. Lett.*, **B693**: (2010), pp. 81–87. DOI: 10.1016/j.physletb.2010.08.011. arXiv: 1006.3575 [hep-ex] (see p. 8).

[23] Georges Aad et al.: **Search for flavour-changing neutral current top-quark decays to qZ in pp collision data collected with the ATLAS detector at $\sqrt{s} = 8$ TeV**. In: *Eur. Phys. J.*, **C76**:1 (2016), p. 12. DOI: 10.1140/epjc/s10052-015-3851-5. arXiv: 1508.05796 [hep-ex] (see p. 8).

[24] Georges Aad et al.: **Search for single top-quark production via flavour-changing neutral currents at 8 TeV with the ATLAS detector**. In: *Eur. Phys. J.*, **C76**:2 (2016), p. 55. DOI: 10.1140/epjc/s10052-016-3876-4. arXiv: 1509.00294 [hep-ex] (see pp. 8, 11).

[25] Georges Aad et al.: **Search for flavour-changing neutral current top quark decays $t \to Hq$ in pp collisions at $\sqrt{s} = 8$ TeV with the ATLAS detector**. In: *JHEP*, **12**: (2015), p. 061. DOI: 10.1007/JHEP12(2015)061. arXiv: 1509.06047 [hep-ex] (see p. 8).

[26] Morad Aaboud et al.: **Search for top quark decays $t \to qH$, with $H \to \gamma\gamma$, in $\sqrt{s} = 13$ TeV pp collisions using the ATLAS detector**. In: (2017). arXiv: 1707.01404 [hep-ex] (see pp. 8, 11).

[27] Albert M Sirunyan et al.: **Search for associated production of a Z boson with a single top quark and for tZ flavour-changing interactions in pp collisions at $\sqrt{s}$ = 8 TeV**. In: (2017). arXiv: 1702.01404 [hep-ex] (see pp. 8, 11).

[28] Serguei Chatrchyan et al.: **Search for Flavor-Changing Neutral Currents in Top-Quark Decays $t \to Zq$ in pp Collisions at $\sqrt{s} = 8$TeV**. In: *Phys. Rev. Lett.*, **112**:17 (2014), p. 171802. DOI: 10.1103/PhysRevLett.112.171802. arXiv: 1312.4194 [hep-ex] (see p. 8).

[29] Vardan Khachatryan et al.: **Search for anomalous single top quark production in association with a photon in pp collisions at $\sqrt{s} = 8$ TeV**. In: *JHEP*, **04**: (2016), p. 035. DOI: 10.1007/JHEP04(2016)035. arXiv: 1511.03951 [hep-ex] (see pp. 8, 11).

[30] Vardan Khachatryan et al.: **Search for top quark decays via Higgs-boson-mediated flavor-changing neutral currents in pp collisions at $\sqrt{s} = 8$ TeV**. In: *JHEP*, **02**: (2017), p. 079. DOI: 10.1007/JHEP02(2017)079. arXiv: 1610.04857 [hep-ex] (see p. 8).

[31] **Search for the flavor-changing interactions of the top quark with the Higgs boson in $H \to b\bar{b}$ channel at $\sqrt{s} = 13$ TeV**. Tech. rep. CMS-PAS-TOP-17-003. Geneva: *CERN*, 2017. URL: https://cds.cern.ch/record/2284743 (see p. 8).

[32] J. A. Aguilar-Saavedra: **A Minimal set of top anomalous couplings**. In: *Nucl. Phys.*, **B812**: (2009), pp. 181–204. DOI: 10.1016/j.nuclphysb.2008.12.012. arXiv: 0811.3842 [hep-ph] (see p. 9).

[33] J. A. Aguilar-Saavedra: **A Minimal set of top-Higgs anomalous couplings**. In: *Nucl. Phys.*, **B821**: (2009), pp. 215–227. DOI: 10.1016/j.nuclphysb.2009.06.022. arXiv: 0904.2387 [hep-ph] (see p. 9).

[34] M. Beneke et al.: **Top quark physics**. In: *1999 CERN Workshop on standard model physics (and more) at the LHC, CERN, Geneva, Switzerland, 25-26 May: Proceedings*. 2000, pp. 419–529. arXiv: hep-ph/0003033 [hep-ph]. URL: http://weblib.cern.ch/abstract?CERN-TH-2000-100 (see p. 9).

[35] Jun Gao, Chong Sheng Li, and Hua Xing Zhu: **Top Quark Decay at Next-to-Next-to Leading Order in QCD**. In: *Phys. Rev. Lett.*, **110**:4 (2013), p. 042001. DOI: 10.1103/PhysRevLett.110.042001. arXiv: 1210.2808 [hep-ph] (see p. 10).

[36] Stephen Myers: **The LEP Collider, from design to approval and commissioning**. John Adams' Lecture. Delivered at CERN, 26 Nov 1990. Geneva: CERN, 1991. URL: http://cds.cern.ch/record/226776 (see p. 13).

[37] Stephen Holmes, Ronald S Moore, and Vladimir Shiltsev: **Overview of the Tevatron collider complex: goals, operations and performance**. In: *Journal of Instrumentation*, **6**:08 (2011), T08001. URL: http://stacks.iop.org/1748-0221/6/i=08/a=T08001 (see p. 13).

[38] R. Barate et al.: **Search for the standard model Higgs boson at LEP**. In: *Phys. Lett.*, **B565**: (2003), pp. 61–75. DOI: 10.1016/S0370-2693(03)00614-2. arXiv: hep-ex/0306033 [hep-ex] (see p. 13).

[39] Kenneth Herner: **Higgs Boson Studies at the Tevatron**. In: *Nucl. Part. Phys. Proc.*, **273-275**: (2016), pp. 852–856. DOI: 10.1016/j.nuclphysbps.2015.09.131 (see p. 13).

[40] Abdelhak Djouadi: **The Anatomy of electro-weak symmetry breaking. I: The Higgs boson in the standard model**. In: *Phys. Rept.*, **457**: (2008), pp. 1–216. DOI: 10.1016/j.physrep.2007.10.004. arXiv: hep-ph/0503172 [hep-ph] (see p. 13).

[41] Lyndon Evans and Philip Bryant: **LHC Machine**. In: *Journal of Instrumentation*, **3**:08 (2008), S08001. URL: http://stacks.iop.org/1748-0221/3/i=08/a=S08001 (see p. 13).

[42] Thomas Sven Pettersson and P Lefèvre: **The Large Hadron Collider: conceptual design**. Tech. rep. CERN-AC-95-05-LHC. Oct. 1995, p. 20 and 22. URL: https://cds.cern.ch/record/291782 (see p. 13).

[43] Jorg Wenninger and Ezio Todesco: **Large Hadron Collider momentum calibration and accuracy**. Tech. rep. CERN-ACC-2017-0007. Geneva: *CERN*, Feb. 2017. URL: https://cds.cern.ch/record/2254678 (see p. 14).

[44] Cinzia De Melis: **The CERN accelerator complex. Complexe des accélérateurs du CERN**. In: (July 2016). General Photo. URL: https://cds.cern.ch/record/2197559 (see p. 14).

[45] G. Aad et al.: **The ATLAS Experiment at the CERN Large Hadron Collider**. In: *JINST*, **3**: (2008), S08003. DOI: 10.1088/1748-0221/3/08/S08003 (see p. 14).

[46] S. Chatrchyan et al.: **The CMS Experiment at the CERN LHC**. In: *JINST*, **3**: (2008), S08004. DOI: 10.1088/1748-0221/3/08/S08004 (see pp. 14, 23).

[47] K. Aamodt et al.: **The ALICE experiment at the CERN LHC**. In: *JINST*, **3**: (2008), S08002. DOI: 10.1088/1748-0221/3/08/S08002 (see p. 14).

[48] A. Augusto Alves Jr. et al.: **The LHCb Detector at the LHC**. In: *JINST*, **3**: (2008), S08005. DOI: 10.1088/1748-0221/3/08/S08005 (see p. 14).

[49] M. Bongi et al.: **Astroparticle physics at LHC: The LHCf experiment ready for data taking**. In: *Nucl. Instrum. Meth.*, **A612**: (2010), pp. 451–454. DOI: 10.1016/j.nima.2009.08.039 (see p. 14).

[50] G. Anelli et al.: **The TOTEM experiment at the CERN Large Hadron Collider**. In: *JINST*, **3**: (2008), S08007. DOI: 10.1088/1748-0221/3/08/S08007 (see p. 14).

[51] B. Acharya et al.: **The Physics Programme Of The MoEDAL Experiment At The LHC**. In: *Int. J. Mod. Phys.*, **A29**: (2014), p. 1430050. DOI: 10.1142/S0217751X14300506. arXiv: 1405.7662 [hep-ph] (see p. 15).

[52] BY JAMES GILLIES: **Luminosity? Why don't we just say collision rate?** In: (Mar. 2011). URL: http://cds.cern.ch/record/1997001 (see p. 15).

[53] BY HARRIET JARLETT and HARRIET KIM JARLETT: **LHC pushes limits of performance**. In: (Aug. 2016). URL: http://cds.cern.ch/record/2212301 (see p. 15).

[54] OLIVER SIM BRÜNING, PAUL COLLIER, P LEBRUN, et al.: **LHC Design Report**. CERN Yellow Reports: Monographs. Geneva: CERN, 2004. URL: https://cds.cern.ch/record/782076 (see p. 15).

[55] JEAN-LUC CARON: **Cross section of LHC dipole.. Dipole LHC: coupe transversale.** AC Collection. Legacy of AC. Pictures from 1992 to 2002. May 1998. URL: https://cds.cern.ch/record/841539 (see p. 16).

[56] **Technical proposal**. LHC Tech. Proposal. Cover title : CMS, the Compact Muon Solenoid : technical proposal. Geneva: CERN, 1994. URL: https://cds.cern.ch/record/290969 (see p. 17).

[57] G. L. BAYATIAN et al.: **CMS physics: Technical design report**. In: (2006) (see pp. 17, 25).

[58] G L BAYATIAN, S CHATRCHYAN, G HMAYAKYAN, et al.: **CMS Physics: Technical Design Report Volume 1: Detector Performance and Software**. Technical Design Report CMS. There is an error on cover due to a technical problem for some items. Geneva: CERN, 2006. URL: https://cds.cern.ch/record/922757 (see pp. 17, 21, 26).

[59] BY CIAN O'LUANAIGH: **LHC progresses towards higher intensities**. In: (Aug. 2015). URL: http://cds.cern.ch/record/2051986 (see p. 17).

[60] CMS COLLABORATION: **Detector Drawings**. CMS Collection. Mar. 2012. URL: https://cds.cern.ch/record/1433717 (see p. 18).

[61] BY CORINNE PRALAVORIO and CORINNE PRALAVORIO: **Major work to ready the LHC experiments for Run 2**. In: (May 2015). URL: http://cds.cern.ch/record/2024977 (see pp. 17, 26).

[62] S CHATRCHYAN, V KHACHATRYAN, A M SIRUNYAN, et al.: **Performance of the CMS Drift Tube Chambers with Cosmic Rays**. In: *J. Instrum.*, **5**:arXiv:0911.4855. CMS-CFT-09-012 (Nov. 2009), T03015 . 47 p. URL: http://cds.cern.ch/record/1223944 (see pp. 19–20).

[63] LUIGI GUIDUCCI: **CMS muon system towards LHC Run 2 and beyond**. Tech. rep. CMS-CR-2014-333. Geneva: *CERN*, Oct. 2014. URL: https://cds.cern.ch/record/1966038 (see p. 20).

[64] CARLO BATTILANA: **The CMS muon system status and upgrades for LHC run-2 and performance of muon reconstruction with 13 TeV data**. Tech. rep. CMS-CR-2016-437. Geneva: *CERN*, Dec. 2016. URL: http://cds.cern.ch/record/2239185 (see p. 20).

[65] SERGUEI CHATRCHYAN et al.: **Performance of CMS muon reconstruction in pp collision events at $\sqrt{s} = 7$ TeV**. In: *JINST*, **7**: (2012), P10002. DOI: 10.1088/1748-0221/7/10/P10002. arXiv: 1206.4071 [physics.ins-det] (see p. 21).

[66] R. Frühwirth: **Application of Kalman filtering to track and vertex fitting**. In: *Nuclear Instruments and Methods in Physics Research Section A: Accelerators, Spectrometers, Detectors and Associated Equipment*, **262**:2 (1987), pp. 444–450. doi: http://dx.doi.org/10.1016/0168-9002(87)90887-4 (see pp. 21, 27).

[67] Pierre Billoir: **Progressive track recognition with a Kalman like fitting procedure**. In: *Comput. Phys. Commun.*, **57**: (1989), pp. 390–394. doi: 10.1016/0010-4655(89)90249-X (see pp. 21, 27).

[68] Emrah Tiras, Burak Bilki, and Yasar Onel: **Commissioning of CMS Forward Hadron Calorimeters with Upgraded Multi-anode PMTs and μTCA Readout**. In: (2016). arXiv: 1611.05232 [physics.ins-det] (see p. 22).

[69] L. Brianza: **Precision crystal calorimetry in LHC Run II with the CMS ECAL**. In: *Journal of Instrumentation*, **12**:01 (2017), p. C01069. url: http://stacks.iop.org/1748-0221/12/i=01/a=C01069 (see p. 24).

[70] Serguei Chatrchyan et al.: **Energy Calibration and Resolution of the CMS Electromagnetic Calorimeter in pp Collisions at $\sqrt{s} = 7$ TeV**. In: *JINST*, **8**: (2013). [JINST8,9009(2013)], P09009. doi: 10.1088/1748-0221/8/09/P09009. arXiv: 1306.2016 [hep-ex] (see p. 24).

[71] Serguei Chatrchyan, Vardan Khachatryan, Albert M Sirunyan, et al.: **Description and performance of track and primary-vertex reconstruction with the CMS tracker**. In: *J. Instrum.*, **9**:arXiv:1405.6569. CERN-PH-EP-2014-070. CMS-TRK-11-001 (May 2014). Comments: Replaced with published version. Added journal reference and DOI, P10009. 80 p. url: http://cds.cern.ch/record/1704291 (see pp. 24, 27).

[72] by Christine Sutton: **Chronicles of CMS: the saga of LS1**. In: (May 2015). url: http://cds.cern.ch/record/2024986 (see p. 26).

[73] **A beautiful barrel for CMS**. In: (Mar. 2014). url: http://cds.cern.ch/record/1998635 (see p. 26).

[74] **Cool running for CMS tracker**. In: (Mar. 2014). url: http://cds.cern.ch/record/1998606 (see p. 26).

[75] K. Rose: **Deterministic annealing for clustering, compression, classification, regression, and related optimization problems**. In: *Proceedings of the IEEE*, **86**:11 (Nov. 1998), pp. 2210–2239. doi: 10.1109/5.726788 (see p. 27).

[76] Wolfgang Waltenberger: **Adaptive Vertex Reconstruction**. Tech. rep. CMS-NOTE-2008-033. Geneva: *CERN*, July 2008. url: https://cds.cern.ch/record/1166320 (see p. 27).

[77] L. Cadamuro: **The CMS Level-1 trigger system for LHC Run II**. In: *Journal of Instrumentation*, **12**:03 (2017), p. C03021. url: http://stacks.iop.org/1748-0221/12/i=03/a=C03021 (see p. 28).

[78] Vardan Khachatryan et al.: **The CMS trigger system**. In: *JINST*, **12**:01 (2017), P01020. doi: 10.1088/1748-0221/12/01/P01020. arXiv: 1609.02366 [physics.ins-det] (see p. 28).

[79] Claudio Grandi, David Stickland, Lucas Taylor, Achille Petrilli, and Alain Hervé: **CMS Computing Model: The "CMS Computing Model RTAG"**. Tech. rep. CMS-NOTE-2004-031. CERN-LHCC-2004-035. LHCC-G-083. Geneva: *CERN*, Dec. 2004. URL: http://cds.cern.ch/record/814248 (see p. 28).

[80] Christoph Eck, J Knobloch, Leslie Robertson, et al.: **LHC computing Grid: Technical Design Report. Version 1.06 (20 Jun 2005)**. Technical Design Report LCG. Geneva: CERN, 2005. URL: https://cds.cern.ch/record/840543 (see p. 28).

[81] S Banerjee: **CMS Simulation Software**. In: *Journal of Physics: Conference Series*, **396**:2 (2012), p. 022003. URL: http://stacks.iop.org/1742-6596/396/i=2/a=022003 (see p. 31).

[82] M Hildreth, V N Ivanchenko, D J Lange, and M J Kortelainen: **CMS Full Simulation for Run-2**. In: *Journal of Physics: Conference Series*, **664**:7 (2015), p. 072022. URL: http://stacks.iop.org/1742-6596/664/i=7/a=072022 (see p. 31).

[83] S. Agostinelli, J. Allison, K. Amako, et al.: **Geant4—a simulation toolkit**. In: *Nuclear Instruments and Methods in Physics Research Section A: Accelerators, Spectrometers, Detectors and Associated Equipment*, **506**:3 (2003), pp. 250–303. DOI: https://doi.org/10.1016/S0168-9002(03)01368-8 (see pp. 31, 33).

[84] Michael H. Seymour and Marilyn Marx: **Monte Carlo Event Generators**. In: *Proceedings, 69th Scottish Universities Summer School in Physics : LHC Phenomenology (SUSSP69): St.Andrews, Scotland, August 19-September 1, 2012*. 2013, pp. 287–319. DOI: 10.1007/978-3-319-05362-2_8. arXiv: 1304.6677 [hep-ph] (see p. 31).

[85] Torbjorn Sjöstrand: **Monte Carlo Tools**. In: *Proceedings, 65th Scottish Universities Summer School in Physics: LHC Physics (SUSSP65): St. Andrews, UK, August 16-29, 2009*. 2009, pp. 309–339. DOI: 10.1201/b11865-14. arXiv: 0911.5286 [hep-ph] (see p. 31).

[86] Stefan Höche: **Introduction to parton-shower event generators**. In: *Proceedings, Theoretical Advanced Study Institute in Elementary Particle Physics: Journeys Through the Precision Frontier: Amplitudes for Colliders (TASI 2014): Boulder, Colorado, June 2-27, 2014*. 2015, pp. 235–295. DOI: 10.1142/9789814678766_0005. arXiv: 1411.4085 [hep-ph] (see pp. 31–32).

[87] Ringaile Placakyte: **Parton Distribution Functions**. In: *Proceedings, 31st International Conference on Physics in collisions (PIC 2011): Vancouver, Canada, August 28-September 1, 2011*. 2011. arXiv: 1111.5452 [hep-ph]. URL: https://inspirehep.net/record/954990/files/arXiv:1111.5452.pdf (see p. 31).

[88] Richard D. Ball, Valerio Bertone, Stefano Carrazza, et al.: **Parton distributions for the LHC run II**. In: *Journal of High Energy Physics*, **2015**:4 (2015), p. 40. DOI: 10.1007/JHEP04(2015)040 (see p. 31).

[89] Jon Butterworth et al.: **PDF4LHC recommendations for LHC Run II**. In: *J. Phys.*, **G43**: (2016), p. 023001. DOI: 10.1088/0954-3899/43/2/023001. arXiv: 1510.03865 [hep-ph] (see p. 31).

[90] Adam Alloul, Neil D. Christensen, Céline Degrande, Claude Duhr, and Benjamin Fuks: **FeynRules 2.0 - A complete toolbox for tree-level phenomenology**. In: *Comput. Phys. Commun.*, **185**: (2014), pp. 2250–2300. doi: 10.1016/j.cpc.2014.04.012. arXiv: 1310.1921 [hep-ph] (see p. 32).

[91] Celine Degrande, Claude Duhr, Benjamin Fuks, et al.: **UFO - The Universal FeynRules Output**. In: *Comput. Phys. Commun.*, **183**: (2012), pp. 1201–1214. doi: 10.1016/j.cpc.2012.01.022. arXiv: 1108.2040 [hep-ph] (see p. 32).

[92] Johan Alwall, Michel Herquet, Fabio Maltoni, Olivier Mattelaer, and Tim Stelzer: **MadGraph 5 : Going Beyond**. In: *JHEP*, **06**: (2011), p. 128. doi: 10.1007/JHEP06(2011)128. arXiv: 1106.0522 [hep-ph] (see pp. 32, 35).

[93] Torbjörn Sjöstrand, Stefan Ask, Jesper R. Christiansen, et al.: **An introduction to {PYTHIA} 8.2**. In: *Computer Physics Communications*, **191**: (2015), pp. 159–177. doi: http://dx.doi.org/10.1016/j.cpc.2015.01.024 (see pp. 32–33).

[94] Torbjorn Sjostrand, Stephen Mrenna, and Peter Z. Skands: **PYTHIA 6.4 Physics and Manual**. In: *JHEP*, **0605**: (2006), p. 026. doi: 10.1088/1126-6708/2006/05/026. arXiv: hep-ph/0603175 [hep-ph] (see pp. 32–33).

[95] Torbjörn Sjöstrand, Stefan Ask, Jesper R. Christiansen, et al.: **An Introduction to PYTHIA 8.2**. In: *Comput. Phys. Commun.*, **191**: (2015), pp. 159–177. doi: 10.1016/j.cpc.2015.01.024. arXiv: 1410.3012 [hep-ph] (see pp. 32–33, 35).

[96] Johan Alwall et al.: **Comparative study of various algorithms for the merging of parton showers and matrix elements in hadronic collisions**. In: *Eur. Phys. J.*, **C53**: (2008), pp. 473–500. doi: 10.1140/epjc/s10052-007-0490-5. arXiv: 0706.2569 [hep-ph] (see p. 32).

[97] J. Alwall, R. Frederix, S. Frixione, et al.: **The automated computation of tree-level and next-to-leading order differential cross sections, and their matching to parton shower simulations**. In: *JHEP*, **07**: (2014), p. 079. doi: 10.1007/JHEP07(2014)079. arXiv: 1405.0301 [hep-ph] (see pp. 32, 35).

[98] Rikkert Frederix and Stefano Frixione: **Merging meets matching in MC@NLO**. In: *JHEP*, **12**: (2012), p. 061. doi: 10.1007/JHEP12(2012)061. arXiv: 1209.6215 [hep-ph] (see p. 32).

[99] Simone Alioli, Paolo Nason, Carlo Oleari, and Emanuele Re: **A general framework for implementing NLO calculations in shower Monte Carlo programs: the POWHEG BOX**. In: *Journal of High Energy Physics*, **2010**:6 (2010), p. 43. doi: 10.1007/JHEP06(2010)043 (see p. 33).

[100] Simone Alioli, Paolo Nason, Carlo Oleari, and Emanuele Re: **NLO single-top production matched with shower in POWHEG: s - and t -channel contributions**. In: *Journal of High Energy Physics*, **2009**:09 (2009), p. 111. url: http://stacks.iop.org/1126-6708/2009/i=09/a=111 (see p. 33).

[101] Stefano Frixione, Paolo Nason, and Carlo Oleari: **Matching NLO QCD computations with parton shower simulations: the POWHEG method**. In: *Journal of High Energy Physics*, **2007**:11 (2007), p. 070. url: http://stacks.iop.org/1126-6708/2007/i=11/a=070 (see p. 33).

[102] Simone Alioli, Paolo Nason, Carlo Oleari, and Emanuele Re: **A general framework for implementing NLO calculations in shower Monte Carlo programs: the POWHEG BOX**. In: *JHEP*, **06**: (2010), p. 043. doi: 10.1007/JHEP06(2010)043. arXiv: 1002.2581 [hep-ph] (see p. 33).

[103] Stefano Frixione, Paolo Nason, and Carlo Oleari: **Matching NLO QCD computations with Parton Shower simulations: the POWHEG method**. In: *JHEP*, **11**: (2007), p. 070. doi: 10.1088/1126-6708/2007/11/070. arXiv: 0709.2092 [hep-ph] (see p. 33).

[104] Paolo Nason: **A New method for combining NLO QCD with shower Monte Carlo algorithms**. In: *JHEP*, **11**: (2004), p. 040. doi: 10.1088/1126-6708/2004/11/040. arXiv: hep-ph/0409146 [hep-ph] (see p. 33).

[105] Andrei V. Gritsan, Raoul Röntsch, Markus Schulze, and Meng Xiao: **Constraining anomalous Higgs boson couplings to the heavy flavor fermions using matrix element techniques**. In: *Phys. Rev.*, **D94**:5 (2016), p. 055023. doi: 10.1103/PhysRevD.94.055023. arXiv: 1606.03107 [hep-ph] (see p. 33).

[106] Ian Anderson et al.: **Constraining anomalous HVV interactions at proton and lepton colliders**. In: *Phys. Rev.*, **D89**:3 (2014), p. 035007. doi: 10.1103/PhysRevD.89.035007. arXiv: 1309.4819 [hep-ph] (see p. 33).

[107] Sara Bolognesi, Yanyan Gao, Andrei V. Gritsan, et al.: **On the spin and parity of a single-produced resonance at the LHC**. In: *Phys. Rev.*, **D86**: (2012), p. 095031. doi: 10.1103/PhysRevD.86.095031. arXiv: 1208.4018 [hep-ph] (see p. 33).

[108] Yanyan Gao, Andrei V. Gritsan, Zijin Guo, et al.: **Spin determination of single-produced resonances at hadron colliders**. In: *Phys. Rev.*, **D81**: (2010), p. 075022. doi: 10.1103/PhysRevD.81.075022. arXiv: 1001.3396 [hep-ph] (see p. 33).

[109] Pierre Artoisenet, Rikkert Frederix, Olivier Mattelaer, and Robbert Rietkerk: **Automatic spin-entangled decays of heavy resonances in Monte Carlo simulations**. In: *JHEP*, **03**: (2013), p. 015. doi: 10.1007/JHEP03(2013)015. arXiv: 1212.3460 [hep-ph] (see p. 33).

[110] V. Khachatryan and etal: **Event generator tunes obtained from underlying event and multiparton scattering measurements**. In: *The European Physical Journal C*, **76**:3 (Mar. 17, 2016), p. 155. doi: 10.1140/epjc/s10052-016-3988-x (see p. 33).

[111] J. Pumplin, D. R. Stump, J. Huston, et al.: **New generation of parton distributions with uncertainties from global QCD analysis**. In: *JHEP*, **07**: (2002), p. 012. doi: 10.1088/1126-6708/2002/07/012. arXiv: hep-ph/0201195 [hep-ph] (see p. 33).

[112] Heribertus B. Hartanto, Barbara Jager, Laura Reina, and Doreen Wackeroth: **Higgs boson production in association with top quarks in the POWHEG BOX**. In: *Phys. Rev.*, **D91**:9 (2015), p. 094003. doi: 10.1103/PhysRevD.91.094003. arXiv: 1501.04498 [hep-ph] (see p. 35).

[113] Tom Melia, Paolo Nason, Raoul Rontsch, and Giulia Zanderighi: **W+W-, WZ and ZZ production in the POWHEG BOX**. In: *JHEP*, **11**: (2011), p. 078. doi: 10.1007/JHEP11(2011)078. arXiv: 1107.5051 [hep-ph] (see p. 35).

[114] Simone Alioli, Paolo Nason, Carlo Oleari, and Emanuele Re: **NLO single-top production matched with shower in POWHEG: s- and t-channel contributions**. In: *JHEP*, **09**: (2009). [Erratum: JHEP02,011(2010)], p. 111. doi: 10.1007/JHEP02(2010)011,10.1088/1126-6708/2009/09/111. arXiv: 0907.4076 [hep-ph] (see p. 35).

[115] Emanuele Re: **Single-top Wt-channel production matched with parton showers using the POWHEG method**. In: *Eur. Phys. J.*, **C71**: (2011), p. 1547. doi: 10.1140/epjc/s10052-011-1547-z. arXiv: 1009.2450 [hep-ph] (see p. 35).